DISS. ETH No. 14854

Charge Writing with an Atomic Force Microscope Tip and Electrostatic Attachment of Colloidal Particles to the Charge Patterns

Dissertation submitted to the
SWISS FEDERAL INSTITUTE OF TECHNOLOGY
ZURICH

for the degree of
Doctor of Technical Sciences

presented by
Patrick Mesquida
Dipl.-Phys.
born April 5, 1971
citizen of the Federal Republic of Germany and the French Republic

accepted upon the recommendation of
Prof. Dr. A. Stemmer, examiner
Prof. Dr. D. Poulikakos, co-examiner

Zurich, 2002

II

Acknowledgments

First, I would like to thank my doctoral advisor Prof. Dr. Andreas Stemmer for making me part of his group and for allowing me great freedom in conducting research at the forefront of nanotechnology.

My further thanks go to Prof. Dr. D. Poulikakos (Laboratory for Thermodynamics in Emerging Technologies, ETH) for acting as co-referee of this thesis.

Particular thanks go to Dr. Helmut Knapp (now CSEM Alpnach), who introduced me to scanning probe methods and shared his large expertise with me.

I appreciated very much the discussion of the results with Dr. Robert Stark and his and Marianne Schindler's proofreading. Furthermore, I thank Guy Birrer for electronic support, Dr. Stefan Blunier (Institute of Mechanics, ETH) for providing silicon samples of various doping levels and Dr. Martin Müller (Laboratory for Electron Microscopy I, ETH) for allowing me to use the SEM and his nice introduction to it.

The following actual or former members of the group must be named as they had to get along with me (in the order of appearance): Shao-Jü Woo, Dr. Markus Brunner, Dr. Jan Frohn, Georg Schitter, Brian Cahill, Daniel Häfliger, Stefan Lengweiler, Dr. Iouri Beliaev, Nicola Naujoks, Dr. Bohuslav Rezek.

Patrick Mesquida
Zurich, May 2002

Contents

Abstract

In addition to established lithographic methods, nanotechnological processes taking place in liquid – as in nature – will increase in importance. A key element thereof is the specific, geometrical functionalisation of surfaces for the targeted fixing of molecules or microscopic particles. In addition to chemical or topographical structuring, electrostatic structuring can be used to achieve this because particles which are dispersed in liquids can be moved and specifically positioned using electric fields.

In this work a new method for generating charge patterns on thin, dielectric films is presented for fixing oppositely charged, colloidal particles to defined locations. To achieve this, positive or negative voltage pulses are applied to a conductive atomic force microscope tip, which is laterally scanned in tapping mode over the sample surface under ambient conditions. Subsequently the sample is immersed in a suspension of nanoparticles for developing the latent, electric pattern.

A resolution of ca. 100 nm (as determined by Kelvin probe microscopy) could be achieved for the electric charge patterns on a thin, teflon-like fluorocarbon film on silicon substrates. The charge decay times were of the order of several hours also at high humidity. The transferred charge quantities were of the order of some 100 up to several 1000 elementary charges per voltage pulse depending on pulse height (20 V – 100 V) and film thickness (20 nm – 200 nm). For a pulse length larger than the oscillation period of the cantilever the charge amounts were independent of the pulse length.

As the charges are neutralised very rapidly on contact with water electrically highly insulating fluorocarbon liquids were used for the particle suspensions. Ultrasonically dispersed gold particles of 20 nm diameter and silica particles of 50 nm diameter could be positioned with a resolution of 500 nm and 1 μm, respectively. The solid particles were thereby trapped within small water droplets resulting from the preparation method. These droplets were triboelectrically charged according to Coehn's rule with positive sign and were attracted by Coulomb force to the negative surface charge patterns.

The resolution and the used materials of the method presented here are not restricted by any principle, so that various applications are conceivable ranging

from the creation of novel, nanostructured surfaces from the liquid phase to the targeted fixing of biological cells.

Kurzfassung

(German abstract)

In der Nanotechnologie werden, neben etablierten lithografischen Methoden, Verfahren an Bedeutung gewinnen, die nach dem Vorbild der Natur in der flüssigen Phase ablaufen. Ein Schlüsselelement ist dabei das gezielte, geometrische Funktionalisieren von Oberflächen, um spezifisch Moleküle oder mikroskopische Partikel zu fixieren. Neben der chemischen oder topografischen bietet sich die elektrostatische Strukturierung an, da Partikel, die sich in Flüssigkeiten befinden, mittels elektrischer Felder bewegt und gezielt positioniert werden können.

In dieser Arbeit wird eine neue Methode vorgestellt, mit der auf dünnen, dielektrischen Filmen Ladungsmuster erzeugt werden, um entgegengesetzt geladene, kolloidale Partikel an definierten Orten zu fixieren. Dazu werden unter Umgebungsbedingungen positive oder negative Spannungspulse an eine leitfähige Rasterkraftmikroskopspitze angelegt, die lateral im Tapping-Mode über die Oberfläche einer Probe gescannt wird. Danach wird die Probe in eine Nanopartikelsuspension eingetaucht, um das latente, elektrische Muster zu entwickeln.

Auf einem dünnen, teflonähnlichen Fluorkohlenstofffilm auf Siliziumsubstraten konnte eine Auflösung von ca. 100 nm (durch Kelvinsondenmikroskopie bestimmt) für die elektrischen Ladungsmuster erreicht werden. Die Ladungszerfallszeiten waren auch bei hoher Luftfeuchtigkeit in der Grössenordnung von mehreren Stunden. Die übertragenen Ladungsmengen waren, abhängig von Pulsspannung (20 V – 100 V) und Filmdicke (20 nm – 200 nm), in der Grössenordnung von einigen Hundert bis mehreren Tausend Elementarladungen pro Spannungspuls. Für eine Pulsdauer grösser als die Oszillationsperiode des Cantilevers waren die Ladungsmengen unabhängig von der Pulsdauer.

Da die Ladungen durch den Kontakt mit Wasser sehr schnell neutralisiert wurden, wurde eine elektrisch hochisolierende Fluorkohlenstoffflüssigkeit für die Partikelsuspension verwendet. Ultraschalldispergierte Goldpartikel mit 20 nm Durchmesser und Siliziumdioxidpartikel mit 50 nm Durchmesser konnten mit einer Auflösung von 500 nm bzw. 1 μm positioniert werden. Die festen Partikel waren dabei in kleine Wassertröpfchen eingeschlossen, die aus der Präparationsmethode resultierten. Diese Tröpfchen waren in Übereinstimmung mit der Coehn'schen Regel triboelektrisch positiv aufgeladen und wurden von negativen Oberflächenladungsmustern mittels Coulombkraft angezogen.

Da diese neue Methode prinzipiell weder im Auflösungsvermögen noch in den verwendeten Materialien eingeschränkt ist, sind vielfältige Anwendungsmöglichkeiten vom Erzeugen nanostrukturierter Oberflächen aus der flüssigen Phase bis hin zum gezielten, elektrostatischen Fixieren von biologischen Zellen denkbar.

Definition of terms

List of symbols

Φ	Potential
x, y	Coordinates parallel to the sample surface
z	Coordinate perpendicular to the sample surface
$\vec{r}$	Spatial position vector
ω	Angular frequency
t	Time
U	Voltage
h	Tip-sample distance
F	Tip-sample force
C	Capacitance
W	Energy
TF	Transfer function
q, Q	Electric charge
a	Effective tip radius
ϵ	Dielectric permittivity
d	Distance of a point charge from the sample surface
σ	Surface charge density
ρ	Electrical resistivity
α	Tip opening angle
f	Cantilever resonance frequency
p	Cantilever oscillation period
τ	Decay time constant
E	Electric field strength
b	Electret layer thickness
B	Bandwidth
K	Conversion factor between Kelvin signal and charge
v_T	Tip velocity
n_S	Number of scan lines per image
R	Particle radius
c	Number concentration of particles
D	Diffusion coefficient
η	Dynamic viscosity
J	Flux of particles
s	Electrode separation

Acronyms

AFM	Atomic Force Microscope/-y
EC	Elementary Charge
FC	Fluorocarbon
FWHM	Full Width at Half Maximum
KFM	Kelvin Probe Force Microscopy

LM	Light Microscope/-y
PECVD	Plasma Enhanced Chemical Vapour Deposition
PFD	Perfluorodecalin
PTFE	Polytetrafluoroethylene
UHQ	Ultrahigh Quality (Water)

Constants

(NIST physical reference data, 1998)

$\epsilon_0 = 8.854187817... \cdot 10^{-12}$ F/m   Electric constant (dielectric permittivity of vacuum)

EC $= 1.602176462(63) \cdot 10^{-19}$ C   Elementary charge

$k_B = 1.3806503(24) \cdot 10^{-23}$ J/K   Boltzmann constant

Chapter 1

Introduction

1.1 Structuring of materials on the micro- and nanoscale

"Can charge writing aid nanotechnological manipulation?" – This was the striking question posed by Wright and Chetwynd as title of a review paper about scanning-probe-based charge writing [Wright98]. But not only since the invention of scanning probe methods considerable efforts have been undertaken to find methods for manipulating and structuring matter on the smallest possible scale. Already since the 50's, when Feynman gave his famous speech, "There's plenty of room at the bottom" [Feynman59], miniaturisation has been driven forward continuously, especially with the lithographic techniques of microtechnology and -electronics. The long-term vision is to "assemble" matter on the atomic scale to obtain full control over the physical and chemical properties of a material. Single atom manipulation – as the ultimate limit – has already been reported in the literature although it is restricted to a very specific system and to special conditions such as vacuum and low temperatures [Eigler90].

Conventional lithographic methods are still far away from this limit of resolution, the best one being the electron beam lithography process, which achieves a resolution of about 5 to 10 nm [Broers96]. Furthermore, lithographic methods are quite expensive and demanding in terms of clean room equipment, vacuum technology, optical systems, etc. and apply only to specific material combinations for the resists, the utilised chemical substances as well as the substrates.

However, in nature, especially in biological systems the build-up of structures on a cellular scale, i.e. in the range of a few micrometres and below, takes place using self-assembly processes thereby achieving a high degree of order without intervention of an operator. It is likely that in the future an important part of micro- and nanostructuring techniques will similarly take place in liquid en-

vironment, which is not compatible with conventional clean room and vacuum techniques. Moreover, these novel techniques will probably take additional advantage of findings from chemistry, biology and materials science, i.e. they will not rely only on downscaling of macroscopic techniques.

For manipulating matter under ambient conditions or in liquids scanning probe methods are very convenient. Due to the small size of the probes, which interact directly with the surfaces, in principle a resolution of a few nanometres can be achieved. Furthermore, the nature of the interaction can comprise a multitude of physical and chemical quantities.

Scanning-probe-based direct mechanical structuring has been performed by scratching or indentation experiments, e.g. on soft polymer surfaces [Jung95]. Local topographical features can also be created by thermomechanical writing using a heated AFM (Atomic Force Microscopy) tip for locally melting a polymer substrate [Mamin92].

The localised deposition of a foreign substance on a surface has been demonstrated by Piner et al. with a method called "Dip-Pen" Nanolithography [Piner99]. They wrote 30 nm wide lines of alkanethiol molecules on a gold film via capillary transport of the molecules from an AFM tip.

Besides the topographical properties the chemical properties of surfaces can also be manipulated with an AFM tip. Maoz et al. have locally functionalised a silane monolayer by oxidation using a biased, conductive AFM tip at ambient conditions [Maoz99]. They obtained polar binding groups, to which a second monolayer was specifically self-assembled achieving a lateral resolution of about 10 nm.

Another example of a chemical reaction locally confined by an AFM tip is a modification of "Dip-Pen" Nanolithography using a Au^{3+}-solution as "ink". Maynor et al. reported the fabrication of sub-100-nm Au structures by localised reduction of Au^{3+} to Au^0 on an Si surface [Maynor01].

The AFM has also been used for directly manipulating small particles. A typical example is pushing colloid-sized particles with the tip [Junno95]. However, this method is not well-suited for targeted processing of materials because of the low operating speed of the AFM, the tip-particle-sticking problems, and the lack of simultaneous visual control.

Electric fields, on the other hand, have proven to be suitable tools for contactless, rapid and parallel manipulation of small particles by using (di)electrophoretic forces such as in electrodeposition [VanderBiest99], in xerography [Mort89] or as in more special applications for creating geometrically defined patterns of colloidal crystals [Hayward00]. In xerography-like experiments Jacobs and Whitesides reported a line width of 2.5 μm for dry, iron oxide powder particles deposited on charge patterns written by application of a bias voltage to metal-coated rubber

stamps in contact with thin poly(methyl methacrylate) (PMMA) films [Jacobs01]. Using indium nanoparticles fabricated in an aerosol generator a resolution of 100 nm line width could be achieved by direct deposition from the gas phase to charge lines, which were generated by contact-electrification with a stainless-steel needle [Krinke01].

Electric fields have several advantages: they can easily be generated not only in vacuum but also in air or in liquids, their strength can be varied flexibly and the polarity can be switched, which is of use for selective manipulation of charged particles. Furthermore, in aqueous solvents the colloidal chemistry is a solid basis for understanding and tuning the electric properties of the systems dealt with.

The electrical patterning of insulating thin-films by scanning-probe-based charge writing has been investigated by several groups already since the early years of the scanning probe era [Stern88]. The main goal was to write "charge dots" by applying voltages to conductive AFM tips and to use the dots as bits for high-resolution encoding of information, thereby overcoming the limitations of magnetic storage techniques, which are due to the finite size of magnetic domains.

Although many different materials suitable for AFM-based charge writing have been found, no attempt was made to use this type of nanoscale charge writing for the attachment of nanoparticles similar to the macroscopic model of xerography [Wright98].

1.2 Motivation and outline of the thesis

The idea that nanoparticles could be attached electrostatically to surfaces which are patterned by charge writing with an AFM tip is picked up as the goal of this thesis: *to develop a procedure for creating topographical structures on dielectric surfaces by attaching colloidal particles to charge patterns written by AFM-based charge storage.*

The method is illustrated in Fig. 1.1. Charges are injected into the sample by applying voltage pulses of defined height and length to a conductive AFM tip, which is scanned laterally over the surface, thereby forming a latent, electric image (a). The sample is then immersed in a nanoparticle suspension (b), and the oppositely charged particles are attracted by the electric field and electrodeposited on the pattern (c).

The principles of this method are similar to the well-known xerography process except for the generation of the latent image, which is done by contact electrification instead of using a photoelectric process. Due to the use of an AFM tip the resolution is not limited by an optical system. Furthermore, the particles are deposited from a liquid instead of using a dry powder.

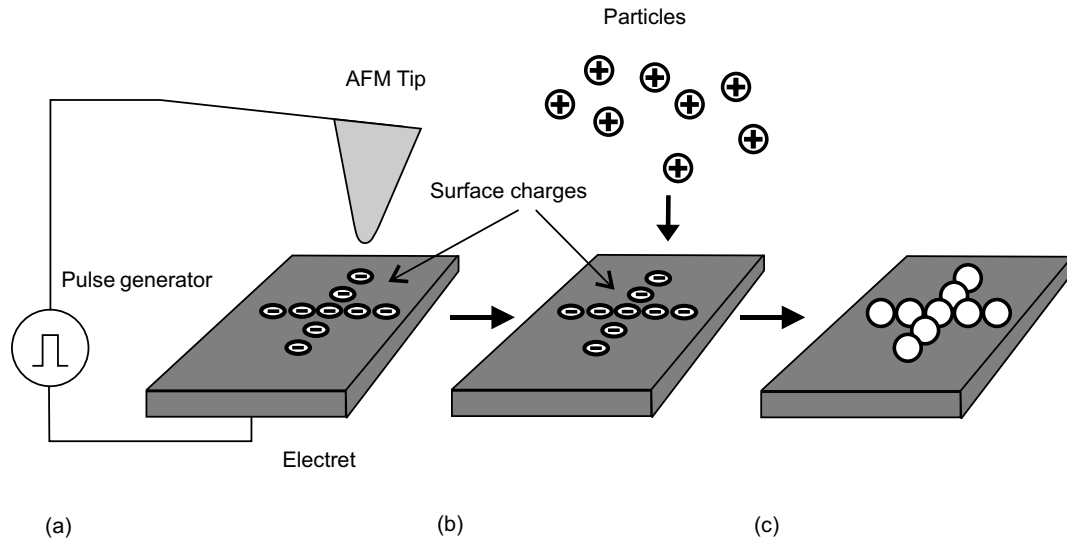This method has a great advantage over mechanically manipulating single

Figure 1.1: **Scheme for nanoparticle attachment.** *Charge writing (a):* Surface charges of arbitrary polarity are written onto an electret by applying voltage pulses to a conductive AFM tip, which is scanned laterally to define the desired pattern. *Dipping (b):* The charged sample is dipped into a suspension of oppositely charged nanoparticles. *Attaching (c):* The nanoparticles are attached by electrostatic attraction to the charge pattern and reproduce the structure defined in (a).

particles one-by-one with the AFM tip. Physically, the charge pattern defines the location where the particles attach on the surface by setting appropriate energetic boundary conditions. Although it is entropically unfavourable for the particles to arrange in an ordered, geometric pattern, the free energy of the system is minimised by a local reduction of the electric potential energy. Thus, after having written the charge pattern, the particles assemble in parallel, without intervention of an operator and thereby without the usually encountered problems of AFM-based, mechanical particle manipulation.

This thesis describes the development and the properties of the method in three major parts:

- Charge detection based on KFM (Kelvin probe force microscopy) is worked out in Chapter 2 describing the physical principles and the resolution limits.

- In Chapter 3 the charge writing is developed. The physics of electrets and the preparation of the samples are described and the technical realisation as well as the results with respect to different experimental parameters are shown.

- The particle attachment is described in Chapter 4. The results of the attachment are shown and discussed for different types of particles with

main focus on the electrostatic attachment mechanism, the resolution and on the suspensions used.

Chapter 2

Kelvin probe force microscopy

Kelvin probe force microscopy (KFM) was used in this work for imaging the charge patterns. With KFM, the surface potential distribution on arbitrary samples (metals, semiconductors or insulators) is measured in non-contact mode. KFM is an application of the traditional Kelvin method ([Ertl74], p.120) for surface potentiometry to the AFM for obtaining sub-μm-resolution. KFM was first introduced 1991 by Nonnenmacher et al. [Nonnenmacher91] and since that time it was utilised, e.g. for the detection of material contrasts [Jacobs97], for imaging potential differences of cell membranes [Knapp02] or for dopant profiling in p-n junctions [Kikukawa95]. A review of the method can be found in the article of Fujihira [Fujihira99].

2.1 Surface potential measurements

2.1.1 Measurement principle

KFM allows the quantitative measurement of the local surface potential, $\Phi_S = \Phi_S(x, y)$, by contactless recording of the electrostatic force between a conductive AFM tip and the sample. To achieve this, the tip is electrically excited at its mechanical resonance frequency, ω, by an AC voltage

$$U(t) = U_{AC} \cos(\omega t) + U_{DC} \qquad (2.1)$$

with amplitude U_{AC} and DC offset U_{DC}. $U(t)$ is applied to the tip held at a distance h above an infinite plane with surface potential $\Phi_S(x, y)$ (Fig. 2.1). If the tip dimensions are small compared to the lateral dimensions of surface features in the potential it can be assumed that $\Phi_S = $ const. This system is basically a capacitor consisting of the two "plates" tip and sample. The potential difference (voltage)
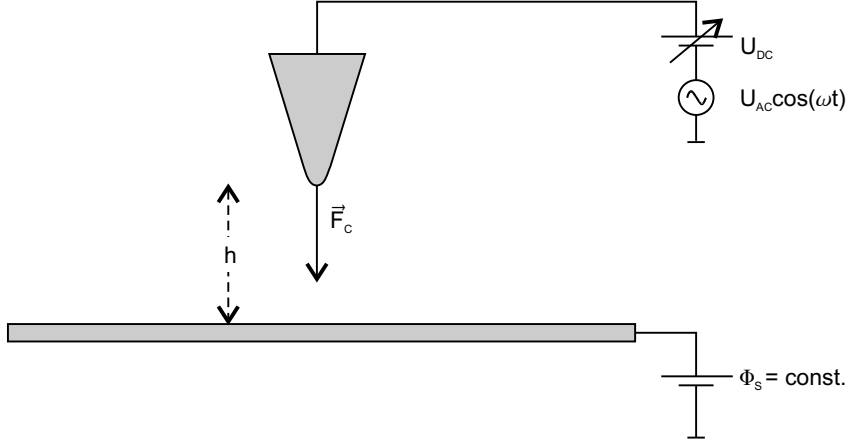
$$U_C = U(t) - \Phi_S \qquad (2.2)$$

Figure 2.1: **Principle of surface potential measurements by KFM.** The ideally conductive tip is kept at potential $U(t) = U_{AC}\cos(\omega t) + U_{DC}$ and is held at distance h from a surface, which potential is kept at Φ_S. The attractive force $\vec{F}_C(t)$ then acts on the tip.

applied to the capacitor leads to an attractive force, $\vec{F}_C$, between tip and sample, which can be derived from the electrostatic energy stored in the capacitive system. The total energy of a capacitance, C, of arbitrary geometry is

$$W = \frac{1}{2}CU_C^2 \ . \tag{2.3}$$

The entire information about the geometry is included implicitly in C. The force, $\vec{F}_C$, is the gradient of W and because of rotational symmetry here, there is only a component along the z-axis

$$|\vec{F}_C| = \left|\frac{\partial W}{\partial z}\right| = \frac{1}{2}\left|\frac{\partial C}{\partial h}\right|U_C^2. \tag{2.4}$$

According to the convention that attractive forces are negative, one can define

$$F_C = \frac{1}{2}\frac{\partial C}{\partial h}U_C^2 \tag{2.5}$$

by taking into account that $\partial C/\partial h$ is negative as $C(h)$ is monotonically decreasing with increasing h. Inserting Eq. 2.2 and Eq. 2.1 yields then

$$F_C = \frac{1}{2}\frac{\partial C}{\partial h}\left(U_{AC}^2\cos^2(\omega t) + (U_{DC} - \Phi_S)^2\right) + \tag{2.6}$$

$$+\frac{\partial C}{\partial h}U_{AC}(U_{DC} - \Phi_S)\cos(\omega t).$$

The ω-component of the force is then

$$\boxed{F_C^\omega = \frac{\partial C}{\partial h}U_{AC}(U_{DC} - \Phi_S)\cos(\omega t).} \tag{2.7}$$

7

In KFM, the amplitude of F_C^ω is recorded by a lock-in amplifier and the Kelvin mode feedback adjusts the offset voltage, U_{DC}, so that $F_C^\omega = 0$ leading to $U_{DC} = \Phi_S$. There were no assumptions made here concerning the tip shape and it is not necessary to know the derivative $\partial C/\partial h$ to obtain the surface potential quantitatively.

Under experimental conditions the Kelvin signal, U_{DC}, corresponds to the contact potential difference, $\Phi_T - \Phi_S$, between tip and sample because the tip also has its own surface potential, Φ_T, depending on the tip material. In metals and semiconductors, Φ_S and Φ_T correspond to the work functions whereas for insulators this quantity is not defined. If measurements are carried out at ambient conditions these values are normally altered by surface contaminations, water and oxide layers as well as by trapped surface charges in the case of insulators [Jacobs99.3].

2.1.2 Resolution and accuracy limits

The lateral resolution and the accuracy of KFM measurements are limited by the finite geometry of the tip. Because of the long range of electric forces the interaction zone between tip and sample is considerably larger compared to the small interaction zone of topographic measurements by AFM. This leads to the observation that small features in the surface potential appear larger and the measured potential appears smaller than they are in reality.

Jacobs and Stemmer [Jacobs99.1] have shown that the total force acting on the tip at a particular point over the sample surface is influenced by different sample regions and represented by mutual tip sample capacitances, C_i (Fig. 2.2). The measured KFM potential is then a weighted average over all potential areas,
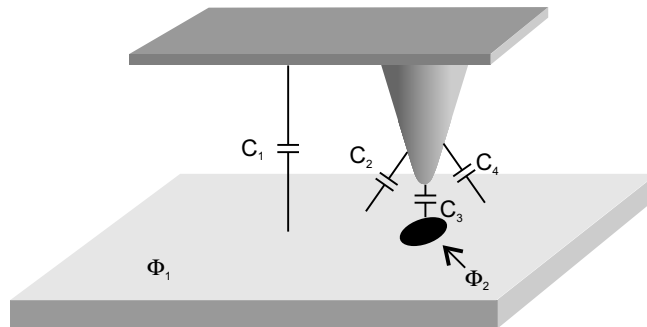

Figure 2.2: **Influence of the finite tip geometry on KFM measurements.** A small surface potential feature located directly below the tip and held at potential Φ_2 contributes only in part to the total force. Sample areas at different potential Φ_1 "smear out" the measured potential by interacting via the local, mutual capacitances C_i.

$$U_{DC} = \frac{\sum_{i=1}^{n} C_i' \Phi_i}{\sum_{i=1}^{n} C_i'} \ , \tag{2.8}$$

the mutual capacitance derivatives, $C_i' = \partial C_i / \partial z$, being the weighting factors. For infinite, flat surfaces, the detected KFM potential is a two-dimensional convolution of the true surface potential distribution with a corresponding transfer function, $TF(x, y)$, defined by the tip geometry [Jacobs99.1].

Numerical simulations using the multiple multipole method and experiments with surface potential features of known geometry showed that the resolution of KFM is limited to about 50 to 100 nm depending strongly on the tip geometry and also on the tip sample distance, h, [Jacobs98]. A point-like potential feature due to, e.g. a point charge at or just below the sample surface (Fig. 2.3) thus would appear as a 50 to 100 nm large structure in the KFM image.
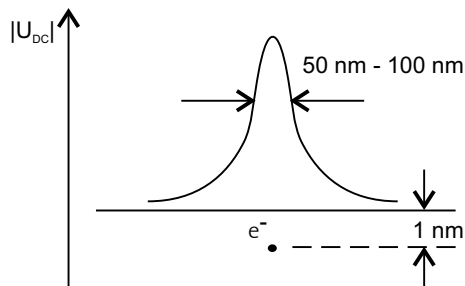

Figure 2.3: **Lateral resolution of a single charge.** U_{DC} is the measured surface potential. An electron, e$^-$, is located 1 nm below the surface.

Belaidi et al. derived the analytical expression

$$res = 2\sqrt{\frac{2}{3}ah} \tag{2.9}$$

for the resolution of electric force microscopy defined by an edge steepness criterion [Belaidi98]. This formula is – for very small distances ($h/a < 0.5$) – in good agreement with electrostatic calculations using the finite element method for a conical tip of spherical apex (radius a) at distance h from a flat sample. With $a = 10$ nm and $h = 5$ nm the theoretical resolution limit becomes $R_e = 12$ nm.

2.1.3 Lift mode

Since the actual tip sample distance, h, affects the potential determination in real KFM measurements all experiments are performed in the so-called lift mode, i.e. each scan line is traced twice (Fig. 2.4). In the first pass the topography is acquired in tapping mode and in the second pass the tip is set at a constant lift height above the sample surface and the KFM measurement is performed.
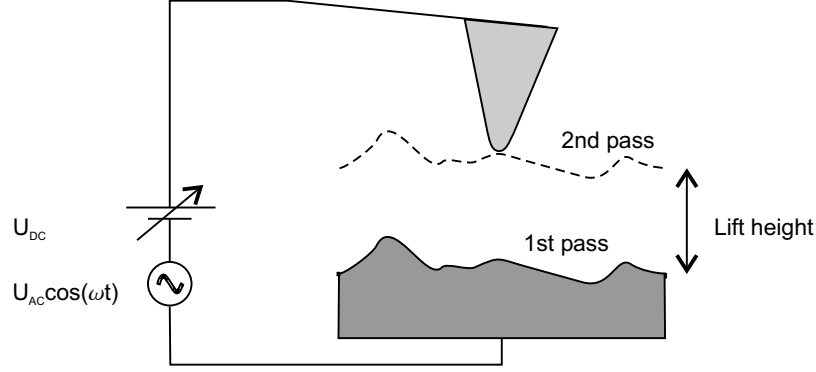
Figure 2.4: **Lift mode.** 1st pass = topography measurement. 2nd pass = potential measurement. The lift height is usually $10\,\text{nm} - 30\,\text{nm}$.

With this method not only artifacts caused by the finite tip geometry are minimised but also the influence of non-electrostatic force contributions such as van-der-Waals forces is at least kept constant during a single measurement. Furthermore, the lift mode allows the quasi-simultaneous measurement of potential as well as of topography with minimal crosstalk.

2.2 Detection of surface charges

Fixed surface charges on the sample alter the local surface potential and can therefore be detected by KFM. A relationship between the Kelvin signal and a surface charge can be established by calculating the force contributions from the tip sample capacitance, F_C, and from the charge, F_Q, separately and by adding them to obtain the total force

$$F = F_C + F_Q. \tag{2.10}$$

F_Q is the Coulombic force between the tip, to which a voltage $U = U(t)$ is applied and a fixed charge, q_S, is placed at distance h (Fig. 2.5). U generates a charge, $q_T = C_T U$, (Fig. 2.5) on the tip ([Sarid94], p.138) and F_Q is then

$$F_Q = \frac{q_T q_S}{4\pi\epsilon_0 (h+a)^2} = \frac{C_T U q_S}{4\pi\epsilon_0 (h+a)^2}. \tag{2.11}$$

C_T is the self-capacitance of the tip and a describes the centroid location of the charge inside the tip as shown in Fig. 2.5. The relative dielectric constant of the medium between tip and sample was set to $\epsilon_r = 1$ because most of the experiments in this work were performed in air. Inserting Eq. 2.1 yields for the
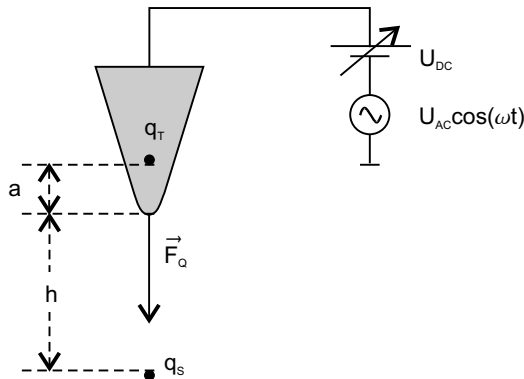
Figure 2.5: **Force contribution of a fixed point charge in KFM.** The point charge q_S is located at distance h from the tip with tip radius a. The virtual charge q_T is generated by U at the centroid location defined by a.

ω-component of F_Q

$$F_Q^\omega = \frac{C_T U_{AC} q_S}{4\pi\epsilon_0 (h+a)^2} \cos(\omega t) \tag{2.12}$$

and adding Eq. 2.12 to Eq. 2.7 and setting the sum to zero finally leads to the result

$$U_{DC} = -\frac{C_T}{4\pi\epsilon_0 (h+a)^2 \frac{\partial C}{\partial h}} q_S + \Phi_S. \tag{2.13}$$

Charge writing and detection experiments are normally performed on flat and chemically homogeneous samples so that $\Phi_S = \text{const.}$ over the whole sample surface. Then Φ_S can be set to zero for the calculation because only variations due to surface charges are of interest.

One sees that the Kelvin signal is proportional to the amount of charge with the proportionality factor depending only on geometrical quantities. The derivative, $\partial C/\partial h$, is negative and the proportionality factor is therefore positive. Thus, positive charges lead to a positive Kelvin signal and vice versa.

The amount of charge cannot be quantitatively determined by KFM without further assumptions on C_T and $\partial C/\partial h$. The quantity q_S has to be accessed by other means, for example by measuring the current during the charge writing. Nevertheless, a quantitative relationship between the Kelvin signal, U_{DC}, and q_S can be found if an appropriate geometrical model for the tip sample system and the capacitances is used.

One of the most commonly used models for calculating tip sample interactions in non-contact mode is that of a sphere with radius a at distance h above an infinite, flat surface (Fig. 2.6). The self-capacitance of a sphere is $C_T = 4\pi\epsilon_0 a$ and the capacitance of the system consisting of a sphere with radius a at height
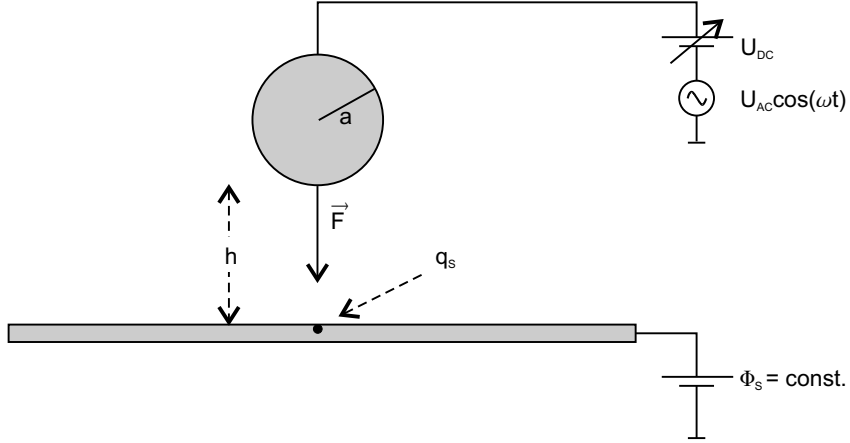
Figure 2.6: **KFM setup with the tip modeled as a conductive sphere.** The tip radius is a.

h above an infinite plane is [Oyama99]

$$C = 4\pi\epsilon_0 a \sum_{n=1}^{\infty} \frac{\sinh(\beta)}{\sinh(n\beta)} \tag{2.14}$$

with $\beta = \ln(1 + \frac{h}{a} + \sqrt{\frac{h}{a}^2 + \frac{2h}{a}})$. For $\ln(h/a) < 1$, Eq. 2.14 can be approximated by [Oyama99]

$$C = -2\pi\epsilon_0 a \ln\left(\frac{h}{a}\right) + \text{const.} \tag{2.15}$$

leading to

$$\frac{\partial C}{\partial h} = -\frac{2\pi\epsilon_0 a}{h}. \tag{2.16}$$

After inserting Eq. 2.16 and C_T into Eq. 2.13 the Kelvin signal becomes

$$U_{DC} = \frac{h}{(h+a)^2 2\pi\epsilon_0} q_S. \tag{2.17}$$

Thus, the proportionality factor between U_{DC} and q_S can be calculated using known quantities and taking a as a geometrical model parameter. The information about the tip sample geometry is now described completely by a. For a real tip, a does not necessarily correspond to the geometric tip radius. To take the long-range electrostatic interactions with the elongated tip into account, a larger "effective" tip radius must be chosen (Fig. 2.7).

To make an estimation whether the model is realistic one can insert typical quantities in Eq. 2.17. The lower limit, i.e. the smallest possible charge, is one
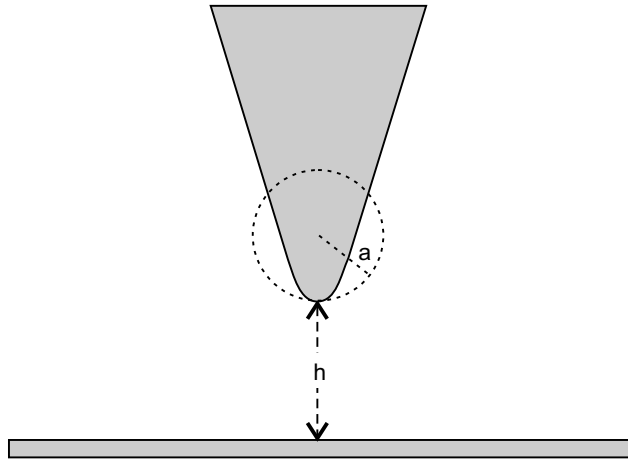
Figure 2.7: **Effective tip radius.** The extended tip geometry can be described by the effective tip radius, a.

single elementary charge (EC), $q_S = 1.6 \cdot 10^{-19}$ C, and with the lift height, $h = 10$ nm, and the tip radius, $a = 10$ nm, one gets

$$U_{DC} = 72 \text{ mV}$$

for the Kelvin signal if the charge was located at the tip surface in the axis of the tip (Fig. 2.6).

This is above the lower detection limit of a carefully adjusted Kelvin microscope meaning that with this method it should ideally be possible to detect single elementary charges at the sample surface. In reality, the potential peak is "smeared out" as indicated in Fig. 2.3 so that the peak in the image appears larger and lower. Therefore, the model must be adapted by choosing a larger effective tip radius.

Jacobs showed that by using the contrast transfer function calculated numerically on the basis of the tip dimensions a potential value of about 20 mV can be expected for a single elementary charge [Jacobs99.2]. An effective tip radius

$$a \approx 30 \text{ nm}$$

is then obtained with Eq. 2.17 and with $h = 10$ nm.

A calculation of the dependence of the measured KFM potential on a for different fixed, localised charges, q_S, reveals the strong influence of the effective tip radius (Fig. 2.8). One sees that especially for 10 nm $< a <$ 40 nm the signal, U_{DC}, strongly depends on a. The dependence is also stronger for increasing charge amount. Therefore, quantitative comparisons of measurements performed with different tips have to be drawn carefully as – in practice – also tips of the same
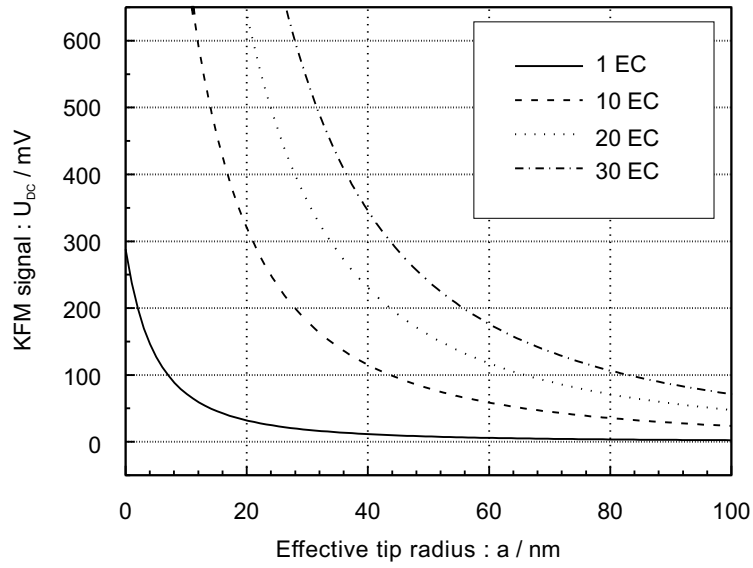
13

Figure 2.8: **Dependence of the measured potential on the effective tip radius.** Theoretical curves of U_{DC} vs. a, calculated with Eq. 2.17 for $q = 1, 10, 20$ and 30 EC, $h = 10$ nm.

kind and from the same manufacturer show variations in the tip apex geometry. Thus, KFM measurements performed with different tips cannot be compared quantitatively without further assumptions.

Chapter 3

Charge writing

The goal of the experiments described in this chapter was to develop and understand the charge writing process as well as to optimise it for the subsequent particle attachment step. Suitable samples for charge storage were prepared and the influence of different, experimental parameters on the charge storage properties was investigated.

3.1 Electrets

According to the definition of Sessler ([Sessler87], p.1) an electret is a dielectric material exhibiting a quasi-permanent electric charge usually characterised by an external, electric field. The term quasi-permanent means that the time constant for charge decay is much longer than the experiment time. There are mainly two classes of electrets: ferroelectrics, which exhibit a permanent polarisation below their Curie temperature, and electrets in the narrower sense, where real charges can be trapped by redistributing electrons within the material or by injecting excess charge carriers into the volume or trapping them at the surface (Fig. 3.1(a)). In this work the second type is dealt with.

The most widely known electrets are carnauba wax, fluorocarbon or hydrocarbon polymers and silicon based multilayer systems [Kressmann96]. Although treated as a scientific curiosity for a long time, many applications have arisen since the 1940's ranging from dosimeters and electret microphones to the widespread xerography. Today, the scientific interest lies especially in electrets in the form of thin-films ([Sessler87], p.1).

Charge generation can be performed by contact electrification with or without applied voltage, by e-beam and by corona charging. Indirect methods are light-, radiation- or heat-induced charge generation ([Sessler87], p.20). The mechanism of charge trapping can be explained by localised trapping levels for charge carriers in the energy diagram (Fig. 3.1(b)). These trapping states are distributed
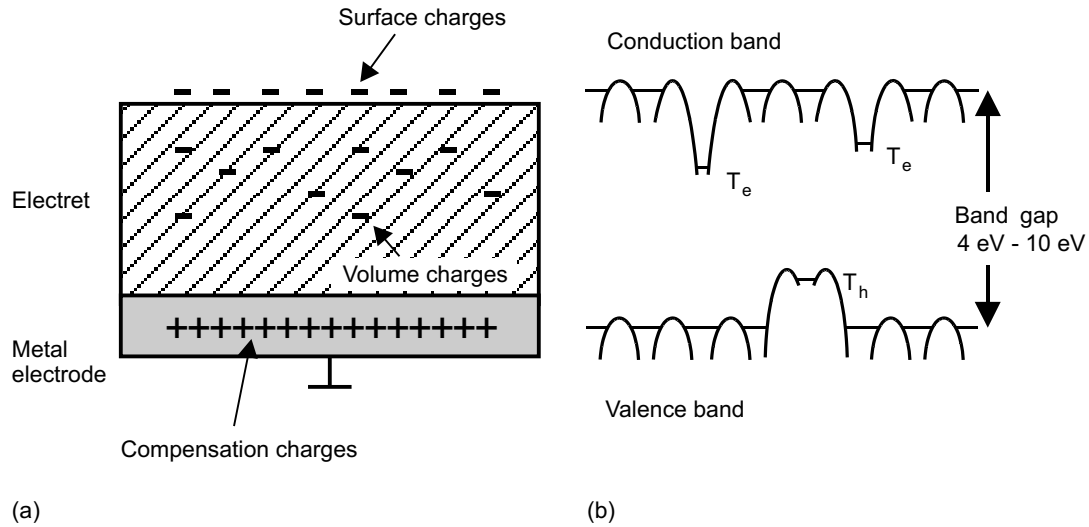
Figure 3.1: **Trapping scheme and energy diagram in polymeric electrets.** (a) Trapping scheme: Real charges are deposited on the surface or injected into the volume of an electret. The charges are often compensated by opposite image charges in a conductive counter electrode. (b) Energy diagram: Electron traps (T_e) and hole traps (T_h) are localised states which can be occupied by or released of electrons, respectively. In the first case, the electret carries a negative net charge and in the second case, the electret carries a positive net charge. As electrets are insulators the band gap is large compared to metals or semiconductors.

randomly reflecting the local, molecular environment in amorphous, poly- or partially crystalline materials. In polymers, the cause of these localised levels are chemical or structural anomalies such as impurities, defects, chain irregularities or imperfections in crystalline regions. Such anomalies are also often located at the electret surface. At high charge densities, internal or external breakdown can occur when the internal or external electric field exceeds the dielectric strength of the material or the surrounding media. Charge decay can be accelerated by increasing the temperature and thereby activating relaxation processes.

One of the best electrets with respect to a high charge storage density and to long charge decay times is polytetrafluoroethylene (PTFE). From theoretical considerations concerning the maximum breakdown field in PTFE foils a maximum surface charge density $\sigma = 4{\cdot}10^{-7}$ C/cm^2, which corresponds to about 25000 elementary charges per μm^2 can be expected ([Sessler87], p.21). The charge retention times were extrapolated to several decades at room temperature ([Sessler87], p.70). These properties, together with the remarkable inertness against almost all kinds of chemicals, make PTFE a promising candidate for charge storage with respect to particle attachment.

Charge writing in PTFE foils was performed 1976 by Feder using electron beam irradiation [Feder76]. The electric structures showed a resolution of about

16

10 μm and the charge density was $\sigma = 6 \cdot 10^{-7}$ C/cm^2 = 37500 EC/μm^2 although being higher than the expected, theoretical limit.

The first experiments concerning high-resolution scanning-probe-based charge writing were conducted in 1988 by Stern et al., who used etched Ni tips to deposit charges on PMMA films [Stern88]. The charging process itself was further investigated with respect to differences between contact- and corona-charging [Schonenberger92]. Several other electrets such as thermally grown SiO$_2$ on Si [Sugawara94] or layered nitride-oxide-silicon (NOS) thin-film structures have been examined since that time [Barrett91]. With NOS layers of 50 nm nitride thickness, feature sizes of ca. 75 to 150 nm were achieved [Barrett91].

In spite of being well-known as an electret, PTFE (as well as other fluorocarbon-based materials) has apparently not been considered as a data storage medium for scanning-probe-based writing although the long decay times are an important argument favouring its use. Because of these advantageous properties and because of its inertness a PTFE-like fluorocarbon (FC) thin-film was used for charge storage and subsequent particle deposition in this work.

3.2 Experimental details

3.2.1 Technical setup and charge writing details

The charge writing, charge detection and topography measurements were performed with a NANOSCOPE MULTIMODE SPM (DIGITAL INSTRUMENTS INC., Santa Barbara CA, USA) equipped with IIIA CONTROLLER for the z- and Kelvin feedback. The EXTENDER ELECTRONICS MODULE served as the phase-sensitive amplifier necessary for the Kelvin ω-component detection.

For KFM, as well as for the charge writing, conductive AFM tips have to be used. Metallised tips often show abrasion of the metal coating during the measurement, which leads to sudden potential jumps in the KFM images [Jacobs99.3]. For this reason, highly doped Si-cantilevers (NSCF 12, NT-MDT CO., Moscow, RUS) with electrical resistivity $\rho < 0.002$ Ωcm, cone opening angle $\alpha < 20°$ and tip apex radius $a < 10$ nm were used in this work. Because these tips can be used both for KFM and charge writing they do not need to be changed between charging and imaging.

The charge writing has been performed by applying voltage pulses of defined height, U_p, and length, t_p, to the cantilever using a custom-built pulse generator (circuit diagram see App. B.1) connected to the tip (Fig. 3.2). The pulse length could be varied from about 0.5 μs to 10 ms and the pulse height from 0 to +60 V with grounded sample mount. For negative charge writing the connection of tip and sample mount has been switched (see App. B.2).
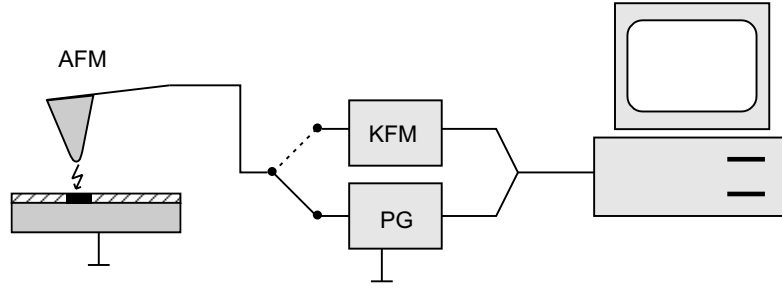
17

Figure 3.2: **Experimental setup.** For charge writing and subsequent KFM measurements the conductive AFM tip is switched between the pulse generator PG and the KFM controller KFM, respectively.

All charge writing experiments were performed in tapping mode with z-feedback turned on. Usually t_p was much longer (about $40\times$) than the oscillation period, p, of the cantilever to ensure that the tip was touching the surface several times during one pulse. The tapping mode turned out to be the most reliable mode for obtaining reproducible results. Applying voltage pulses in contact mode often led to a damaged tip or sample surface or produced no charge transfer at all.

The controlled, lateral motion of the cantilever for writing defined patterns was achieved by three different methods depending on the total structure size and complexity:

1. Small structures (< 10 μm) consisting of only a few, distinguishable charge "dots" (Fig. 3.3(a)) were written by moving the tip to the specified dot location, then applying one single voltage pulse and then moving the tip to the next location. The tip was laterally moved using the internal lithography programming language of the NANOSCOPE software and the voltage pulses were triggered individually (see App. B.4).

2. Intermediate structures ($\approx$ 10 μm $-$ 30 μm) such as continuous lines (Fig. 3.3(b)) were written by first moving the tip to the starting point and then starting a continuous pulse sequence at fixed pulse frequency, during which the tip is drawn along the line at a defined velocity. At the ending point of the line the pulse sequence was stopped.

3. For larger structures (> 30 μm) the internal lithography mode showed too much drifting and hysteresis. The best results were obtained by running the normal AFM topography scanning motion and turning the pulse generator on and off manually at the desired positions. With this method, only simple geometric structures such as single or crossed rectangles, whose width was determined by the actual scan size, could be written (Fig. 3.3(c)).
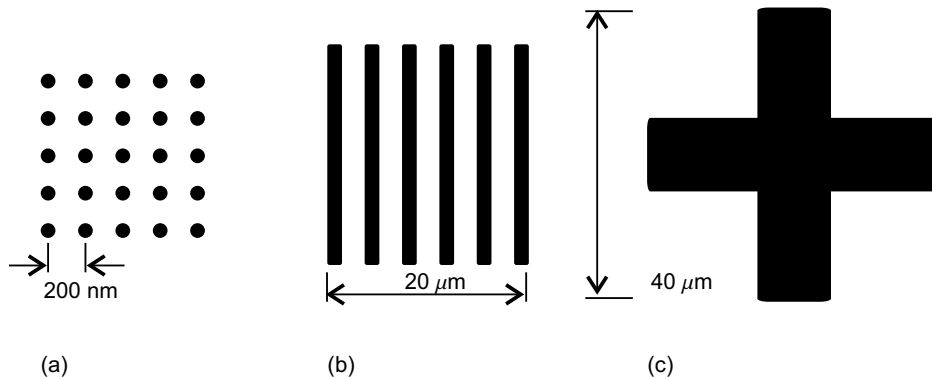
Figure 3.3: **Charge writing templates.** The NANOSCOPE lithography mode was used in (a) with 1 dot = 1 pulse and in (b) with 1 line = 1 sequence of pulses. In (c) the x-y-scanning was left enabled and pulse sequences were manually activated at the desired positions.

All experiments were performed under ambient conditions (relative humidity $30\% - 40\%$, temperature $20°C - 25°C$) except for those concerning the influence of humidity (Sec. 3.3.6) and those performed in liquid environment (Sects. 3.4.2 and 3.4.1). For the experiments at variable humidity the AFM head was equipped with a case connected to a flow pipe, with which the relative humidity could be adjusted from 6 to 98 % [Knapp99]. The charge writing and detection in liquid environment was performed using the NANOSCOPE liquid cell.

The quantitative analysis of the experiments was performed by measuring the peak height as well as the full width at half maximum (FWHM) of the KFM signal images of single dots consisting of deposited charges as sketched in Fig. 3.3(a). According to Eq. 2.17 the KFM signal, $\Phi = U_{DC}$, is proportional to the total charge amount, q, present below the tip with the proportionality factor depending on the tip sample distance, h, and the effective tip radius, a. For a better accuracy a statistical evaluation has been made by averaging over 25 dots (as shown in Fig. 3.3(a)) for fixed U_p and t_p.

3.2.2   Preparation of samples

All experiments were performed using samples consisting of a thin-film FC electret layer on a conductive, smooth substrate such as p-doped Si or Au. The FC layers were prepared by Plasma Enhanced Chemical Vapour Deposition (PECVD). For the PECVD, a custom-built plasma chamber [Knapp98] with hexafluoropropene (CF_3–CF=CF_2) as precursor gas was used (Fig. 3.4). The plasma was generated by a 2 kV$_{pp}$ AC-voltage at $5 \cdot 10^{-2}$ hPa chamber pressure. The growth rate was determined to about 10 nm/min [Wicki01]. The substrates had previously been cleaned with the same apparatus in an air plasma to remove hydrocarbon contaminations from the surface.
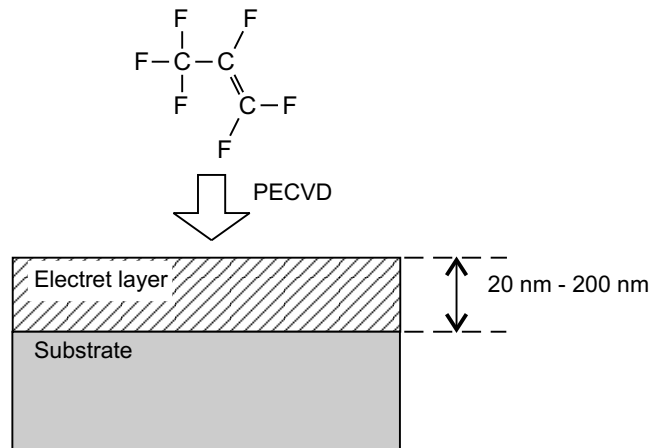
19

Figure 3.4: **PECVD preparation of FC samples.** CF_3–CF=CF_2 is used as precursor gas for coating different substrates with a PTFE-like FC layer.

X-ray photoelectron spectroscopy (XPS) investigations showed that the composition of the so-produced FC layers differ from PTFE consisting only of C and F atoms [KnappPriv]. The FC layers also contain a certain amount of H atoms (probably from residual water and hydrocarbon molecules in the cell) and from the XPS peaks the following ratios of different carbon bonds were determined:

$$CF_3 : CF_2 : CF : HCF : CH \approx 14 : 27 : 26 : 26 : 7.$$

The high relative amount of CF-bonds indicates a high degree of crosslinking in the polymer. This molecular structure probably improves the charge trapping capability because of the high number of imperfections leading to localised trapping states.

The dielectric constant has not been determined but experiments with similar PECVD-produced fluorocarbon layers [Uhlig00] showed that $\epsilon_r = 2.0 - 2.7$ depending on the deposition parameters. This low value is of use for the fabrication of low-voltage integrated circuits where suitable dielectrics with a dielectric constant lower than that of SiO_2 ($\epsilon_r = 3.9$) are sought.

3.3   Results of charge writing in air

3.3.1   Charge dot patterns

Charge writing with positive as well as with negative voltage pulses is demonstrated by KFM images (Fig. 3.5 (b) and (d)) taken directly after writing. The lithography mode was used for writing single charge dots arranged to form the letters "ETH" of 1-μm-size and of a resolution of about 100 nm.
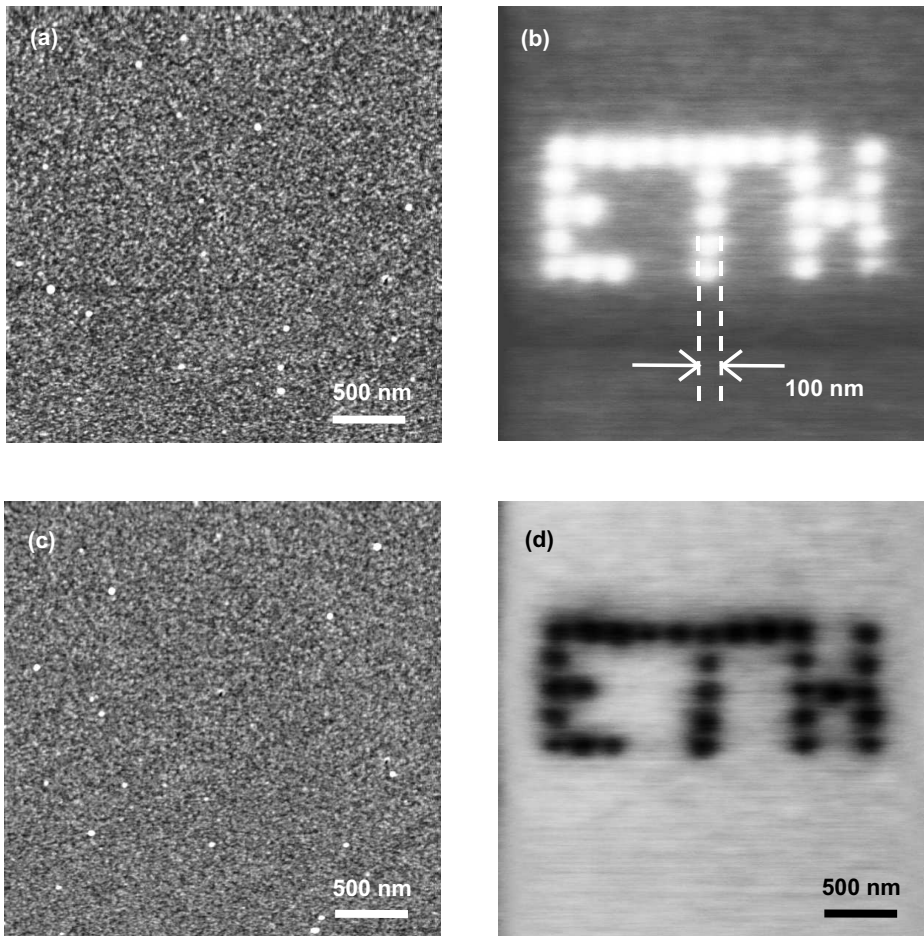
Figure 3.5: **"ETH" symbol consisting of localised surface charges.** Positive and negative charge "dots" written into a 30-nm-thick fluorocarbon layer on Si substrate. (a) and (c) Topography of the area corresponding to the KFM images (b) and (d) respectively. Topography z-range 10 nm, potential range 1 V, $U_p = +45$ V in (b) and $U_p = -45$ V in (d), $t_p = 5$ μs. Bright (dark) parts correspond to positive (negative) surface potential in (b) and (d), the zero potential reference values are different in (b) and (d).

In the topographic images (a) and (c) the grains of the FC material can be seen. There is no correlation between topography and KFM images, indicating that the charge writing does not damage the surface.

A resolution of 100 nm could be achieved only with the best tips. On average, the resolution in the KFM images in terms of the FWHM of charge dots was about 200 nm (Fig. 3.6 and Sec. 3.3.2). It is assumed that this is not a limit set by the charge writing process because the lateral resolution of KFM is in the range of 50 to 100 nm depending on the tip geometry (Sec. 2.1.2).

Fig. 3.6 shows KFM images of positive and negative charge dots of the first
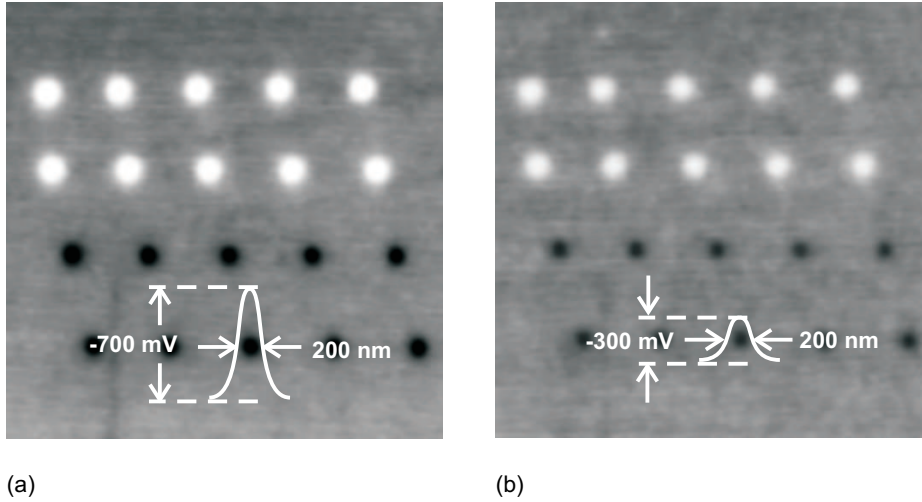
(a)   (b)

Figure 3.6: **KFM images of charge pattern decaying due to multiple scanning.** Sample: 30-nm-thick FC layer on Si Substrate (not the same sample as shown in Fig. 3.5), in air at ambient conditions, $U_p = +45$ V (bright dots), $U_p = -45$ V (dark dots), $t_p = 1$ ms, image size 6 μm × 6 μm, potential range 2 V, (a) 1st scan, (b) 12th scan.

scan (a) as well as of the 12th scan (b) after charge writing. Imaging several times consecutively the particular charge pattern led to a decrease of the KFM signal of more than 50 %, which was not observed if only one single image was taken after 1 h, the time needed for recording 12 images.

In Fig. 3.7 the decrease of the KFM signal, $|U_{DC}|$, on continuous scanning is shown for positive as well as for negative charges. The lines are exponential decay fits, $|U_{DC}| \propto \mathrm{e}^{-n/n_e}$, of the experimental data (n : scan number), which yield decay constants $n_e = 3.5 \pm 0.5$ for the positive charges and $n_e = 2.8 \pm 0.6$ for the negative charges.

This indicates that the charges of both polarities are located right at or very close to the surface. They are being collected back by the AFM tip during scanning because in KFM measurements the tip is kept at ground potential by the instrument during the first pass of each scan line (Sec. 2.1.3).

Furthermore, the charge dots did not show any lateral spreading after the charge writing (Fig. 3.6). Obviously, the hydrophobic FC material [Knapp99] prevents water condensation at the surface and thereby inhibits lateral charge migration due to the electrical conductivity of a possible water film.

3.3.2 Dependence on voltage pulse height

To examine the voltage dependence of the stored charge amount and the resolution, U_{DC} and $FWHM$ are plotted against U_p (Fig. 3.8). A possible influence of
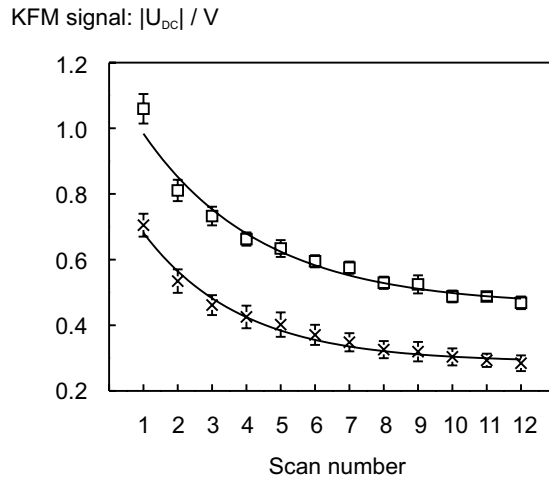
KFM signal: $|U_{DC}|$ / V

Figure 3.7: **Charge decay on multiple scanning.** Sample: 30-nm-thick FC layer on Si Substrate (same sample and tip as in Fig. 3.6), in air at ambient conditions, $U_p = +45$ V($\square$), $U_p = -45$ V($\times$), $t_p = 1$ ms, all measurements were performed with the same tip. The lines are 1st-order-exponential fits using $|U_{DC}| \propto e^{-n/n_e}$, ($n$ = scan number, n_e = decay constant).

t_p was checked by performing the same experiment at two different pulse lengths.

Fig. 3.8(a) shows that the amount of charge that can be stored depends on the applied voltage but not on the pulse length. U_{DC} shows a polarity symmetric, almost linear behaviour between about -1500 mV for $U_p = -60$ V and $+1500$ mV for $U_p = +60$ V. The threshold voltage, U_T, i.e. the lowest U_p for which charge dots could be detected, is about ± 20 V. The dot size also varies linearly with U_p from ca. 250 to 400 nm (Fig. 3.8(b)).

An estimation of the transferred charge amount can be made using the geometric model introduced in Sec. 2.2 (Fig. 2.6). As a first approximation it is assumed that the charges are located on the film surface and are concentrated to one single point. Thus, the charge amount, q_S, can be calculated from U_{DC} with Eq. 2.17

$$q_S = \frac{(h+a)^2 2\pi\epsilon_0}{h} U_{DC}. \tag{3.1}$$

The effective tip radius, a, is difficult to assess. As stated before (Sec. 2.2) numerical calculations suggest $a = 30$ nm and with $h = 10$ nm the calculated charge is

$$q_S = 6 \text{ EC } (83 \text{ EC})$$

for $U_{DC} = 0.1$ V ($U_{DC} = 1.5$ V). According to this estimate only a small charge amount of the order of 1 to 100 EC is transferred into the electret. These values give a good idea of the magnitude of the transferred charge but they always have
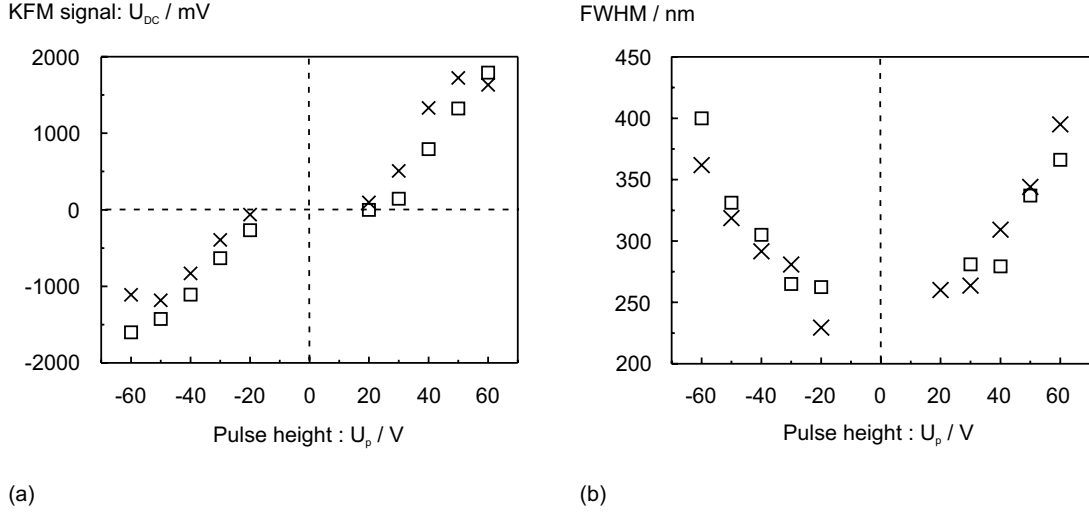
23

Figure 3.8: **Dependence of the stored charge amount on the pulse height.** (a) Charge amount measured by U_{DC} vs. U_p, (b) dot size described by $FWHM$ vs. U_p, $\times : t_p = 1$ ms, $\square$: $t_p = 5$ μs, film thickness $b = 30$ nm, substrate p-doped Si ($\rho = 1$ Ωcm $- 5$ Ωcm), in air at ambient conditions, standard deviation $\delta U_{DC} = 100$ mV, $\delta FWHM = 50$ nm, all measurements were performed with the same tip.

to be subjected to a critical analysis because of the strong influence, $O(a^2)$, of a in the calculation and because image charges are induced in an adjacent counter electrode thereby lowering the measured Kelvin signal.

3.3.3   Charge amount: Direct measurements

If the amount of charge could be measured quantitatively and independently, a relationship between U_{DC} and q could be established. With $q = 1000$ EC and $t = 1$ μs the pulse current of single voltage pulses is

$$I_p = q/t \approx 160 \text{ pA}$$

assuming that $I_p = $ const. during t_p. Such a small current cannot be measured directly on the microsecond scale because commercial amperemeters with pA-sensitivity are restricted to (quasi)-DC measurements [Keithley98].

An alternative is the measurement of the voltage drop over a series resistor in the pulse circuit. A large resistance of the order of 100 MΩ is necessary to obtain sufficiently high voltage signals of the order of 10 mV. Unfortunately, high resistances show a high thermal noise signal ($R_m = 100$ MΩ, bandwidth $B > 1$ MHz and $T = 300$ K)

$$U_{rms} = \sqrt{4k_B T R_m B} > 1 \text{ mV}.$$

Furthermore, high-impedance measurements can only be performed using a measurement amplifier with a much higher input impedance in the $T\Omega$-range.

However, as only the total, transferred charge amount per voltage pulse is sought it is not necessary to measure the time-resolved signal run, $I_p(t)$. Instead, an integration over I_p was performed and for improving the sensitivity and the accuracy the integration is performed over a large number of voltage pulses, N, at constant pulse parameters, U_p and t_p, thereby increasing the signal-to-noise ratio. To achieve this an analog integrator consisting of a high-speed JFET operational amplifier with input impedance in the $T\Omega$-range has been coupled to a series resistor with $R_m = 1\,G\Omega$ in the pulse circuit (Fig. 3.9, the exact electronic configuration of the integrator is described in App. B.3).
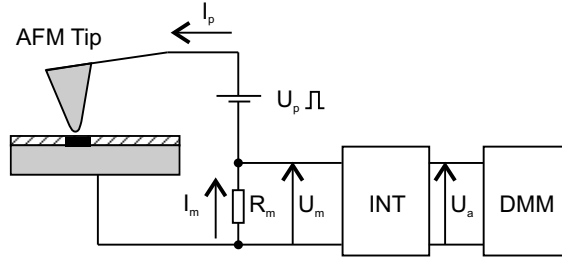

Figure 3.9: **Measurement of the charge amount by integration.** A series resistor R_m is inserted into the charge writing circuit between the counter electrode (substrate) and the pulse generator (U_p). The current, I_m, through R_m generates a voltage drop, U_m. This signal is integrated over a defined time, t, by the analog integrator (INT). The output signal, U_a, is measured by a digital multimetre (DMM) or an oscilloscope. INT has a high input impedance so that $I_m \approx I_p$.

The output signal, U_a, of the analog integrator follows the time law

$$U_a(t) = \frac{1}{t_{INT}} \int_0^t U_m(t')\delta t' = \frac{R_m}{t_{INT}} \int_0^t I_p(t')\delta t' \tag{3.2}$$

with integrator time constant, t_{INT}, which is given by the device configuration, and with $I_p(t') \approx I_m(t')$. The total, transferred charge is

$$q_{tot}(t) = \int_0^t I_p(t')\delta t' \tag{3.3}$$

and the transferred charge per pulse is then

$$q_p(t) = \frac{q_{tot}(t)}{N(t)} = \frac{t_{INT}U_a(t)}{R_m N(t)} \tag{3.4}$$

with the number, $N(t)$, of voltage pulses applied during the integration time, t.

After careful adjustment of the integrator, the measurement was performed as follows without changing the tip:

1. About 33000 voltage pulses were applied to a 128 μm $\times$ 128 μm area on a 100-nm-FC layer on Si substrate at fixed U_p and t_p with the method shown in Fig. 3.3(c). The charge dots were placed at mutual distances of about 1 μm to avoid multiple charging. The output value, $U_a^{(1)}$, was recorded by a digital multimetre (DMM) or an oscilloscope.

2. After zeroing the integrator the procedure was immediately repeated without changing the electric circuit configuration but with retracted and secured tip. When secured, the tip is positioned at about 15 μm above the sample surface thereby preventing charge transfer. The non-zero offset output, $U_a^{(2)}$, was recorded and subtracted from $U_a^{(1)}$.

3. The series resistor was removed and a KFM measurement was performed to obtain U_{DC}-values for comparison.

Statistical errors and noise were considerably reduced by the integration in the first step whereas the second step was performed to minimise systematic error signals, which accumulate during the integration.

Tab. 3.1 shows the results of charge measurements for four different parameter combinations of U_p and t_{INT}. The values of q_p were calculated with $U_a = U_a^{(1)} - U_a^{(2)}$ using Eq. 3.4. U_{DC} was independently recorded by KFM. The high-impedance resistor used here is specified to 1 GΩ($\pm$10 %).

U_p/V	t_{INT}/ms	U_a/V	q_p/EC	U_{DC}/V	K/(EC/V)
+60	68.0 $\pm$ 0.680	0.1 $\pm$ 0.01	1290 $\pm$ 270	1 $\pm$ 0.1	1290 $\pm$ 400
+60	6.8 $\pm$ 0.068	1.0 $\pm$ 0.01	1290 $\pm$ 160	1 $\pm$ 0.1	1290 $\pm$ 290
+80	6.8 $\pm$ 0.068	2.7 $\pm$ 0.01	3480 $\pm$ 400	1.45 $\pm$ 0.1	2400 $\pm$ 440
+100	6.8 $\pm$ 0.068	2.9 $\pm$ 0.01	3730 $\pm$ 430	1.55 $\pm$ 0.1	2400 $\pm$ 430
				Average value for K	1850 $\pm$ 640

Table 3.1: **Direct measurement of the charge amount written by single voltage pulses.** Sample: 100-nm-FC layer on Si, $t_p = 1$ ms, U_a = measured value at the integrator output after offset correction, q_p = charge per pulse calculated with Eq. 3.4, U_{DC} = KFM signal, $K := q_p/U_{DC}$.

The measured values of q_p are in the range of 1000 to 4000 EC, which is much higher than the estimated value from Sec. 3.3.2. This result can be attributed to several limitations of the simple model described by Eq. 2.17, which is valid only for surface charges. Although the results obtained in Sec. 3.3.1 suggest that the charges are located mainly at the surface other experiments have shown that charge carriers can penetrate several micrometres into PTFE ([Sessler87], p.30). If a charge carrier, q_V, is located within the volume of the FC layer its contribution to the KFM signal is smaller than at the surface, where it can be

represented by an "effective" surface charge, $q'_S < q_V$ (see App. A). Furthermore, excess charges present in the film or at the surface induce opposite image charges in the highly conducting substrate, which lowers the electric field experienced by the tip for a given charge quantity.

An additional argument against very small charge amounts of the order of only a few EC is that discrete values of U_{DC} have never been observed in the experiments. As the spatial distribution of trapped charge carriers in the film is not known the true charge amount cannot be calculated with Eq. 2.17 without further assumptions but for given film thickness, tip radius and material properties the independently measured quantity K can be used for calibrating KFM measurements.

The upper limit for the trapped charge amount can be assumed to be given by the maximum surface charge density $\sigma_{max} = 25000\ \mathrm{EC}/\mu\mathrm{m}^2$ of PTFE ([Sessler87], p.21). If the charge $q = 4000$ EC is concentrated within a circular area of 1 μm diameter the surface charge density can be computed to

$$\sigma = 4q/(\pi FWHM^2) \approx 5100\ \mathrm{EC}/\mu\mathrm{m}^2,$$

which is much lower than σ_{max}. Thus, the values obtained for q_p by direct measurements are within reasonable theoretical limits.

3.3.4 Dependence on film thickness

The influence of the film thickness, b, on the trapped charge amount was investigated by measuring U_{DC} vs. U_p for $b = 20$ nm, 100 nm, and 200 nm. Fig. 3.10 shows that the charge storage properties are different for positive and negative voltages especially in the case of thicker films. For positive U_p the KFM signal reaches a value of up to 3500 mV whereas for negative U_p the signal does not exceed -1500 mV. Obviously, more positive than negative charge can be stored for the same $|U_p|$. This can be attributed to different penetration depths for positive and negative charge carriers in an FC electret ([Sessler87], p.30). In this case, the total amount of positive charge that can be stored is higher than that of negative charge for a given $|U_p|$.

Furthermore, the results in Fig. 3.10 show that the threshold voltage, U_T, increases with b. This is due to the film-thickness-dependent electric field, $\vec{E}$, between the tip and the grounded counter electrode for a given U_p (Fig. 3.11). The release of charge carriers takes place first at the part of the tip surface with the highest radius of curvature, which is the tip apex, where a certain minimum field strength $|\vec{E}_T|$ corresponding to $|U_T|$ must be given. With increasing b the distance between tip and counter electrode increases and the pulse voltage necessary for reaching $|\vec{E}_T|$ must be increased. Thus, with regard to particle attachment it is necessary to generate the highest possible surface fields, i.e. thick FC layers and
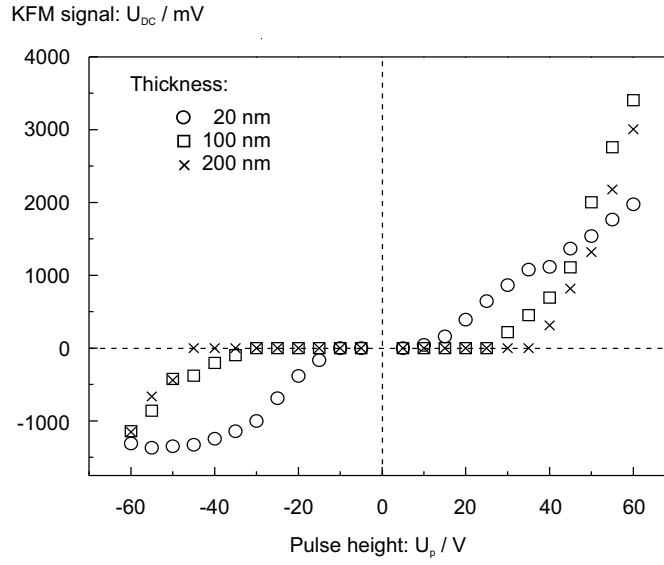
Figure 3.10: **Film thickness dependence of the charge writing.** KFM signal U_{DC} vs. U_p for different film thicknesses, $t_p = 100~\mu s$, substrate p-doped Si ($\rho = 1~\Omega\text{cm} - 5~\Omega\text{cm}$), in air at ambient conditions, standard deviation $\delta U_{DC} = 100$ mV. All values were measured with the same tip.
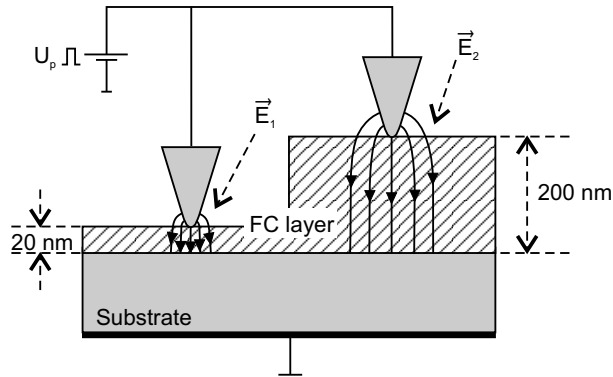
Figure 3.11: **Electric field in the FC layer.** The electric field $\vec{E}$ depends on the film thickness at fixed U_p. The conductive substrate acts as the counter electrode. Here $|\vec{E_1}| > |\vec{E_2}|$ at the tip apex.

high U_p must be used.

28

3.3.5 Dependence on voltage pulse length

According to Fig. 3.8 the transferred charge amount at given pulse height, U_p, does not depend on the pulse length for 5 μs $< t_p <$ 1 ms. Obviously, the entire charge transfer takes place within the first microseconds even for longer voltage pulses. Nevertheless, more detailed investigations show a t_p-dependence for short pulse lengths, $t_p < p = 1/f$, with the cantilever tapping period, p, and resonance frequency, $f = \omega/2\pi$.

Fig. 3.12 shows KFM images of 25-dot charge patterns written on the same sample at $U_p = 45$ V for $t_p < p$ (a) and for $t_p > p$ (b). Fig. 3.12(a) shows that

(a)   (b)
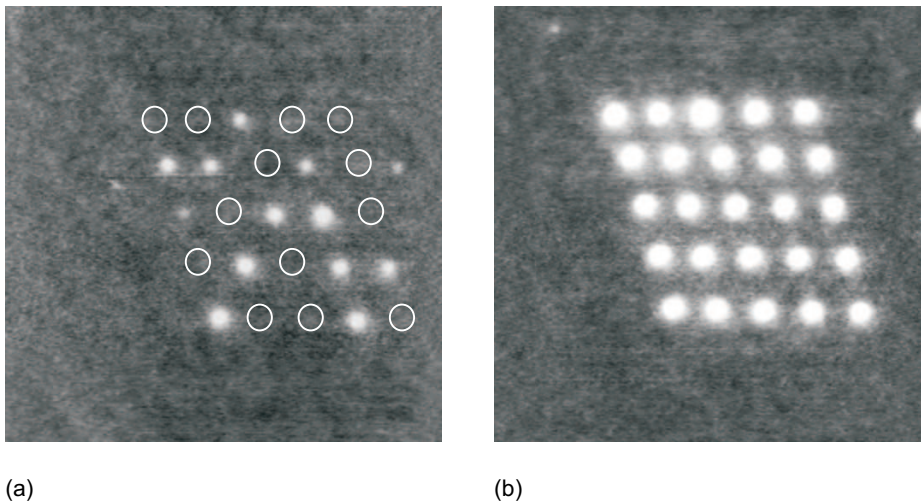
Figure 3.12: **Pulse length dependence (KFM images).** KFM images of 25 charge dots, signal range 0.5 V, scan size 10 μm $\times$ 10 μm, $b = 30$ nm, substrate p-doped Si ($\rho = 1$ Ωcm $-$ 5 Ωcm), $U_p = +45$ V, in air at ambient conditions, cantilever tapping period $p = 25.9$ μs, (a) $t_p = 2$ μs, (b) $t_p = 27$ μs. The circles in (a) indicate the positions where voltage pulses were applied but no charge dots could be detected. The distortion of the charge patterns is due to scanner drifts during the charge writing.

some of the voltage pulses were not "successful" (circles) whereas voltage pulses applied at $t_p > p$ (Fig. 3.12(b)) were always "successful". For taking into account the probability of a successful charge transfer the respective average of all 25 KFM signal peaks including the zero-values for the non-successful voltage pulses was calculated for a range of t_p-values as shown in Fig. 3.13. The measurement series of U_{DC} vs. t_p were performed for two different cantilevers of different resonance frequencies $f = 177$ kHz and $f = 39$ kHz showing that for $t_p < p$ the average KFM signal decreases with decreasing t_p whereas for $t_p \geq p$ the KFM signal is independent of t_p.

This correlation with p can be explained if one assumes that charge is transferred only if the tip is in contact with the sample surface. Since the transfer time
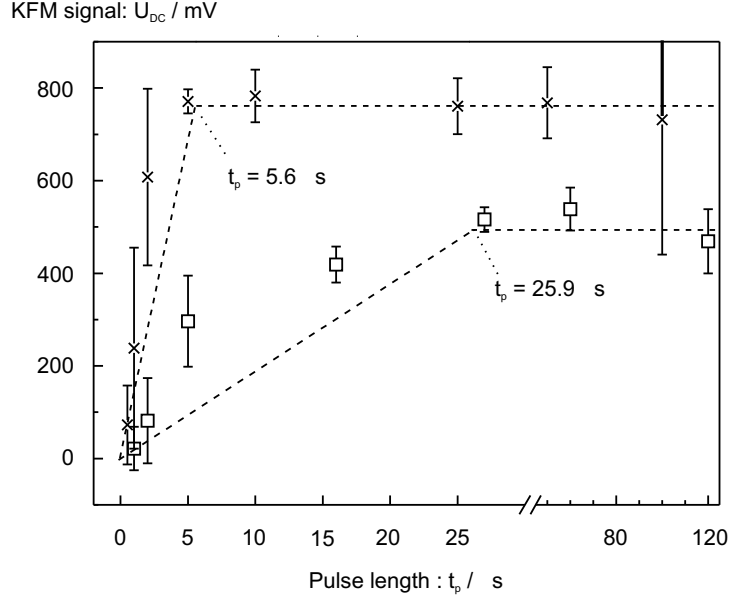
29

KFM signal: U_{DC} / mV

Figure 3.13: **Pulse length dependence of the charge writing.** KFM signal U_{DC} (averaged) vs. t_p for two different cantilevers with resonance frequencies $f = 177$ kHz($\times$) and $f = 39$ kHz($\square$), $U_p = 45$ V, $b = 30$ nm, substrate p-doped Si ($\rho = 1$ Ωcm $- 5$ Ωcm), in air at ambient conditions. The two highlighted t_p-values correspond to the cantilever tapping periods $p = 1/f$. Dashed lines: Expected linear increase for $t_p < p$ and constant value for $t_p \geq p$. Note the break in the x-axis scale.

is probably very small for such small charge amounts the entire transfer occurs at the first impact after starting the voltage pulse (Fig. 3.14 "Charge transfer"). If $t_p < p$ the probability that the impact occurs during the pulse scales with t_p/p since the pulses and the tip oscillation phase are not correlated in time. However, if $t_p > p$ the probability of an impact during the pulse is 1 and the charge is transferred for all pulses.

Theoretically, the average values of U_{DC} should lie on the dashed lines shown in Fig. 3.13 where the probability is taken as a weighting factor. However, there is a slower decrease with decreasing t_p, which is presumably caused by the perturbation of the cantilever tapping motion. The electric field which is applied during the voltage pulse bends the cantilever towards the sample leading to a higher probability of successful charge transfer for $t_p < p$. Thus, for an optimum charge "yield" the pulse length always has to be chosen larger than the tapping period of the particular cantilever.
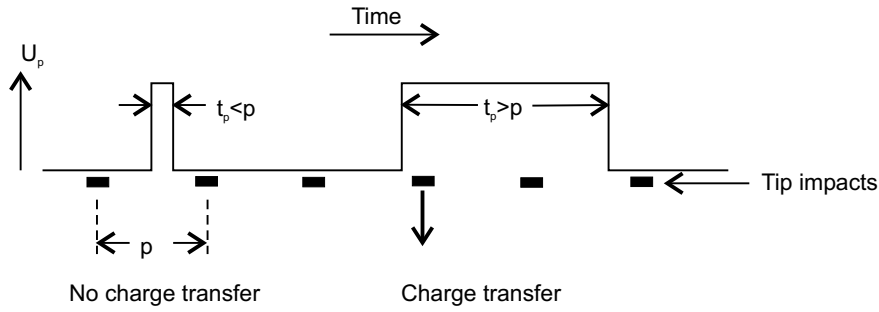
Figure 3.14: **Charge transfer.** The entire charge transfer takes place within a very short time period only on tip sample contact. The bars indicate the impacts ("taps") of an unperturbed cantilever in tapping mode with period p. If a short pulse of $t_p < p$ does not occur at the same time as the tapping impact no charge is transferred. If $t_p > p$ the probability of charge transfer is 100 %.

3.3.6 Charge decay: Influence of humidity

Although it is known that trapped charges remain stable in PTFE for a very long time (see Chapter 3.1 and [Sessler87], p.70) it is not clear whether this is also the case in the PECVD-produced FC layers. There are several reasons of a possible charge decay, which are usually classified into two groups: external and internal charge decay (Fig. 3.15).
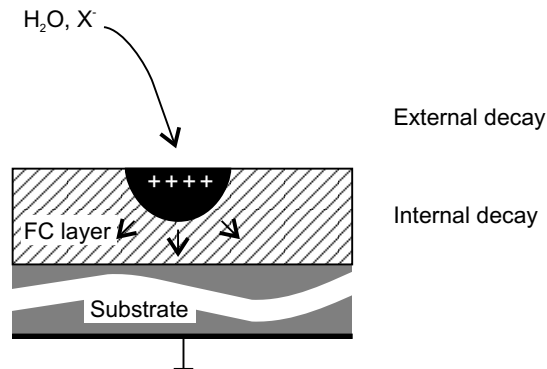
Figure 3.15: **Charge decay mechanisms.** External decay: Ion adsorption from the surroundings and influence of the electrical conductivity of the surrounding medium. Internal decay: Ohmic drift and thermal diffusion.

The external decay is due to the neutralisation of surface charges, which can be caused by the adsorption of counterions from the surrounding medium or by charge loss due to its electrical conductivity. In the case of air as environment the amount of available counterions and the electrical conductivity are both influenced by the humidity. Ions are always generated by radioactive background

31

radiation. The external contribution can only be quantified by comparison with charge decay measurements in perfect vacuum and/or with shielded samples.

The internal decay is caused by the small but non-zero electrical conductivity of the electret material and by diffusion of charge carriers. Excess charges are subjected to drifts caused by their own fields. Diffusion plays mostly a minor role in charge decay ([Sessler87], p.60).

The influence of the environment, especially of the humidity of the surrounding air, was investigated using the setup shown in Fig. 3.16. By varying the ratio
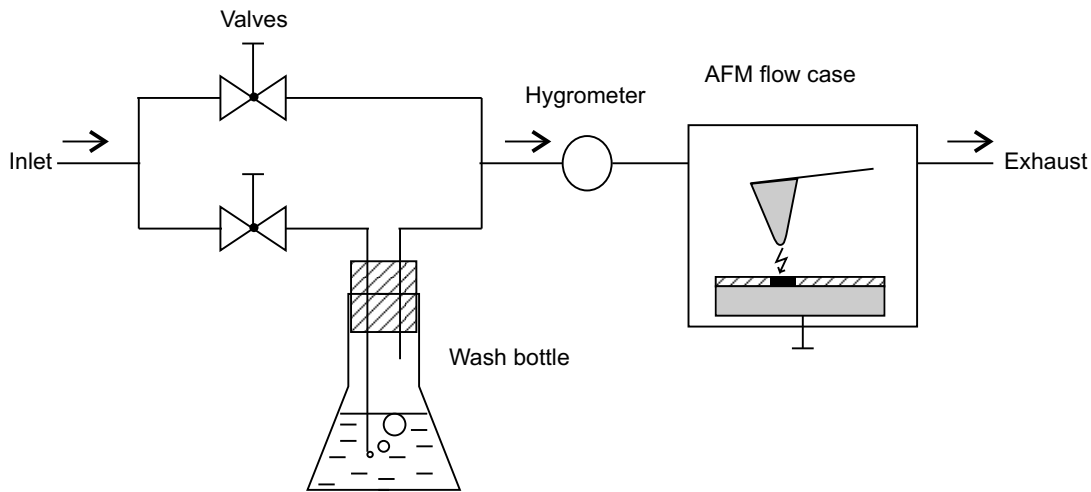

Figure 3.16: **Setup for measurements under controlled humidity.** The AFM head is equipped with a flow case allowing a small, controlled air flow through the head without disturbing the measurements. The inlet is connected to the pressurised air supply of the laboratory, which has an almost constant humidity of 6 %. By adjusting the two valves the ratio of air flowing through the wash bottle filled with water can be controlled so that the maximum humidity of the air flowing through the case is between 6 and 98 %.

of dry air from the central air supply and of air flowing through the wash bottle the humidity of a fine air flow through the capsuled head of the AFM could be adjusted between 6 and 98 %. The charge decay was measured at constant humidity by writing charge dots for given U_p and t_p as shown in Fig. 3.3(a). Then the sample was left in the AFM for the time t until a KFM image of the charge pattern was recorded. The whole procedure was performed for different times, t, always writing a new charge pattern.

The results of the charge decay measurement at 98 % air humidity are shown in Fig. 3.17(a). The initial KFM signal decreases rapidly within the first half an hour and shows an exponential decay down to zero after about 13 h. These experimental data can be fitted by an exponential decay law with two decay constants (continuous line in Fig. 3.17(a)). If one assumes that there are two
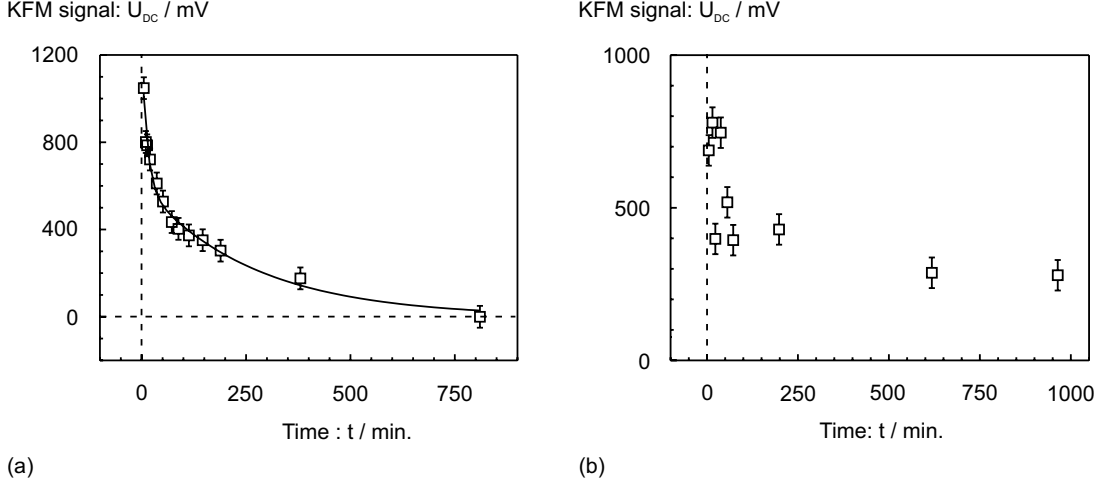
KFM signal: U_{DC} / mV
KFM signal: U_{DC} / mV

(a)

(b)

Figure 3.17: **Influence of the humidity on the charge decay.** KFM signal U_{DC} vs. time t, (a) humidity = 98 %, (b) humidity = 6 %, $b = 30$ nm, substrate p-doped Si ($\rho = 1$ Ωcm $- 5$ Ωcm) , $U_p = 25$ V, $t_p = 100$ μs. The line in (a) is a fit using two exponential decay functions.

independent sorts of trapped charges, $q^{(1)}$ and $q^{(2)}$, the total charge is

$$q(t) = q_0^{(1)} \mathrm{e}^{-t/\tau_1} + q_0^{(2)} \mathrm{e}^{-t/\tau_2} \tag{3.5}$$

and the corresponding time law for the KFM signal is

$$U_{DC}(t) = U_0^{(1)} \mathrm{e}^{-t/\tau_1} + U_0^{(2)} \mathrm{e}^{-t/\tau_2} \tag{3.6}$$

with the initial KFM signal $U_0^{(1)} + U_0^{(2)}$ for $t = 0$. The exponential fit with Eq. 3.6 yields the time constants $\tau_1 = 13$ min and $\tau_2 = 266$ min.

The occurrence of two different time constants can be explained by the existence of surface charges, which are predominantly subjected to external charge decay, and volume charges, which are predominantly subjected to internal decay. However, from these measurements it is difficult to determine the ratio of surface and volume charges and it cannot be specified which decay process is faster.

As the internal charge decay is not affected by a change of the environmental conditions the measurement was repeated at low humidity (6 %). The results are shown in Fig. 3.17(b). A fit cannot be performed with the experimental data because during the first hour after charge writing the values show too much fluctuation. This can be attributed to the high number of available ions in dry air, which are attracted by the external electric field of the charged sample and which are randomly trapped on the surface thereby altering the KFM signal of the charge dots. Similar problems of sudden, unwanted charge trapping on biological membranes at low humidity have been reported by Knapp [KnappPriv]. However,

33

it can be seen in Fig. 3.17(b) that a KFM signal of about 40 % of the initial signal at $t = 0$ could be detected after more than 15 h.

Additional experiments with charged samples kept in closed petri dishes under normal laboratory conditions, i.e. 30 to 40 % humidity at room temperature, showed that the charges could still be detected after more than one week illustrating the excellent charge storage properties of this PTFE-like fluorocarbon material.

3.3.7   Charge decay: Influence of substrate

For investigating a possible charge decay due to ohmic leakage through the substrate two samples of the same film thickness $b = 30$ nm were prepared with p-doped Si ($\rho = 1$ Ωcm $- 5$ Ωcm) and Au substrate, respectively. The Au film was prepared by sputtering Au onto Si substrate and electrically connecting the Au film to ground. The decay measurements were performed in the same way as described in the previous section at normal laboratory conditions without flow case. Fig. 3.18 shows that the charge decay is faster with the Au substrate
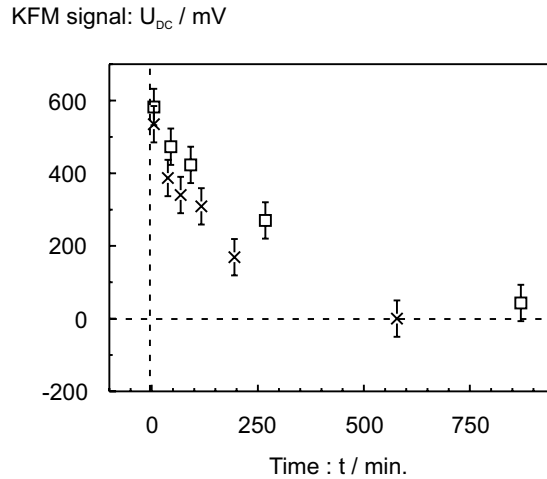
Figure 3.18: **Influence of the substrate on the charge decay.** KFM signal U_{DC} vs. t, $b = 30$ nm, $\square$: Si substrate ($\rho = 1$ Ωcm $- 5$ Ωcm), $\times$: Au (grounded) substrate, $U_p = 25$ V, $t_p = 100$ μs, in air at ambient conditions.

than with the Si substrate. With Si substrate, charges could still be detected after more than 14 h whereas with Au substrate, no charges could be detected anymore after 10 h.

This leads to the conclusion that a certain quantity of volume charges leaks through the substrate. Nevertheless, a metal can also be used as electret substrate allowing a flexible choice for practical applications. Additionally the results with

FC on Au prove that the charges are stored within the FC layer and not in the thin, native SiO_2-layer of Si.

3.3.8 Artifacts

In this section, two other practical aspects of the method are briefly described. As charge writing always includes a current flow as well as relatively high electric fields at the tip apex, the sample or the tip can be damaged.

Fig. 3.19 shows such sample damages which occasionally occur in the FC electret. In both cases, the charge writing was performed at $U_p = 45$ V $- 50$ V

(a)   (b)
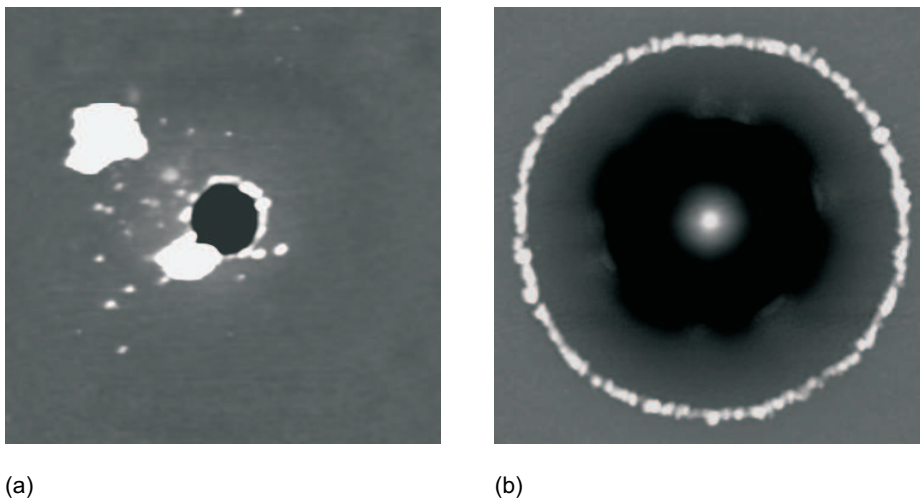
Figure 3.19: **Damage of the sample surface.** Topography images of holes torn in FC films on Si substrate during charge writing: (a) $b = 30$ nm, $U_p = 45$ V, $t_p = 60$ μs, z-range $= 20$ nm, (b) $b = 90$ nm, $U_p = 50$ V, $t_p = 1$ ms, z-range $= 100$ nm. Both images taken in air at ambient conditions, scan area $= 5$ μm $\times$ 5 μm.

and a part of the electret material appears to be molten and/or torn out of the layer. If the transition impedance between tip and sample is very high, it can lead to a large heat generation and thereby to a partial melting of the electret.

Furthermore, a dielectric breakdown can occur in thin dielectric films even at relatively low voltages because the distance between tip and counter electrode is small. For example, the electric field between two capacitor plates at distance $h = 100$ nm and voltage $U = 50$ V is

$$E = U/h = 5 \cdot 10^6 \text{ V/cm},$$

which is of the order of the dielectric strength of PTFE ($2.2 \cdot 10^6$ V/cm, [Sessler87], p.21). Moreover, the electric field lines are concentrated at the tip apex due to the high curvature radius.

Another effect sometimes occurring is the sudden loss of charge writing capability of a particular tip, although KFM measurements still are possible. An explanation would be the local oxidation of the tip material due to the current flow (Fig. 3.20). If a substantial oxide layer is present at the tip apex the con-
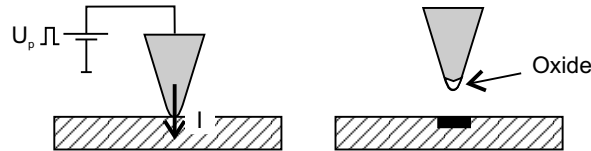

Figure 3.20: **Oxidation of tip material.** The electric current flow can lead to an oxidised tip. KFM measurements are still possible but the charge transfer is blocked by the oxide layer.

tact resistance between tip and sample would be too high and charge transfer is blocked. KFM measurements, on the other hand, are still possible because KFM is a potential respectively a force measurement without current flow.

3.4 Results of charge writing in liquids

3.4.1 Charge loss in liquids

The influence of different liquids on the stability of the charge patterns has been investigated as follows (Fig. 3.21):

1. Positive and negative charge patterns consisting of 40 μm × 10 μm rectangular areas similar to Fig. 3.3(c) were written on a 150-nm-thick FC layers in air at normal conditions and subsequently imaged by KFM (Fig. 3.21(a),(b)).

2. The charged sample was immersed in the liquid for 2 min (Fig. 3.21(c)).

3. After removing the sample from the bath and evaporation of the remaining liquid by blowing with dry air the charge patterns were re-imaged and the KFM signal was compared to that before immersion.

In order to assume a well defined immersion time, the samples were taken out of the AFM after the first KFM measurement and were put into a small glass dish filled with the respective liquids. The approximate positions of the charge patterns on the samples were manually marked by scratches in the FC layer to facilitate the localisation of the patterns after immersion.

Five different liquids of three types – water, two hydrocarbons and two fluorocarbons – were compared. The water was of ultrahigh quality with an electrical resistivity of 18 MΩcm produced by a commercial UHQ apparatus (ELGASTAT
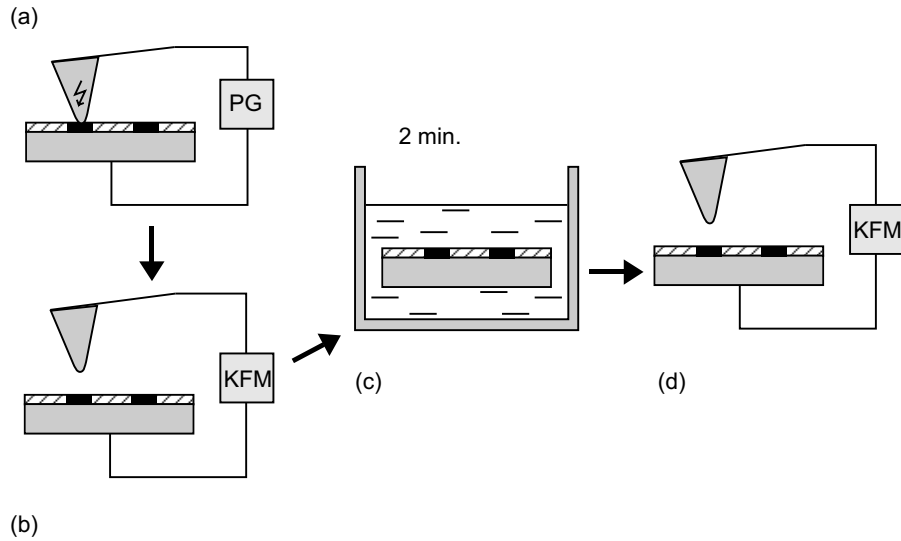
Figure 3.21: **Influence of different liquids on charge decay.** Positive and negative charge writing (a), imaging by KFM (b), immersion in the liquid for 2 min (c), re-imaging by KFM (d). Samples: 150-nm-thick FC layer on Si substrate, $U_p = \pm 55 - \pm 60$ V, $t_p = 1$ ms.

UHQ II, ELGA LTD., Bucks, UK). Heptane (n-C_7H_{16}) of analytical grade (puriss., > 99.5 %, water content ≤ 0.005 %, FLUKA CHEMIE GMBH, Buchs, CH) as well as of technical quality (≥ 95 %, centralised chemical supply, CHEMISTRY DEPT., ETH ZURICH) was chosen as rapidly evaporating hydrocarbon. Although pure heptane has a very high electrical resistivity of the order of 10^{16} Ωcm the lower hydroalkanes are sensitive to organic contaminations and water uptake, which significantly lowers their electrical resistivity. Two different grades of heptane have been used for investigating the influence of the purity grade.

The two fluorocarbons perfluorodecalin (PFD, $C_{10}F_{18}$) and FC-77, which consists of a mixture of n-perfluoroalkanes with an average molecular weight of 415, have been used because of their high electrical resistivity of about 10^{15} to 10^{17} Ωcm, their insensitivity to organic and aqueous contaminations and their complete inertness.

In Tab. 3.2 the remaining percentage of the KFM signal after 2 min immersion is listed for the five liquids. Positive (+) as well as negative (−) charge patterns have been investigated separately. In all cases the charge patterns could still be found again but with UHQ water and with technical heptane only a small part of 4 to 7 % of the initial KFM signal was recorded. For heptane (puriss.) the remaining value was 53 %. For the two perfluorocarbons, on the other hand, there was practically no charge decay within the 2-min-immersion. In all cases no difference between positive and negative charge decay could be measured.

Liquid	$\rho/\Omega\mathrm{cm}$	$+$	$-$
UHQ-Water	$18 \cdot 10^6$	4%	4%
Heptane (techn.)	$1 \cdot 10^{16}$	7%	7%
Heptane (puriss.)	$1 \cdot 10^{16}$	53%	53%
PFD	$1 \cdot 10^{17}$	98%	98%
FC-77	$1.9 \cdot 10^{15}$	98%	98%

Table 3.2: **Charge decay in liquids.** Percentage of the KFM signal after 2 min immersion of the sample in the liquid. The area-averaged KFM signal of positive ($+$) and negative ($-$) charged areas of 40 μm $\times$ 10 μm charge patterns was measured before and after immersion. PFD = $C_{10}F_{18}$, FC-77 = mixture of perfluoroalkanes (see App. B.5.2), ρ = electrical resistivity of the liquid (see App. B.5.2).

UHQ water obviously neutralises most of the surface charges within the short immersion time. This indicates a location of positive as well as negative charge carriers at or close to the surface and supports the results obtained in Sec. 3.3.1. The high charge decay in heptane can be explained by its sensitivity to contaminations as indicated by the significant difference depending on the purity. Even when using the purest grade the liquid is probably contaminated by the immersion of the sample itself.

3.4.2 Charge writing and detection in liquids

For reducing the number of process steps charge writing and particle attachment could be performed within the AFM liquid cell simultaneously without removing the sample. In the case of water charge writing might be possible but KFM measurements for checking the written patterns cannot be performed because of the conductivity of water, which causes a short circuit between cantilever and sample or substrate (Fig. 3.22). Furthermore, the dielectric constant of water decreases the KFM signal sensitivity by a factor of 81 (Eq. 2.17). In insulating liquids, on the other hand, the detection of charge patterns by KFM is possible and for PFD or FC-77 a dielectric correction factor of only $1-2$ has to be applied.

In Fig. 3.23 charge writing and detection in PFD using the liquid cell is demonstrated. PFD has a high viscosity and a low vapour pressure, which reduces the perturbing liquid flows within the cell and prolongates the measurement time until evaporation of the liquid. After re-tuning the cantilever to its shifted resonance frequency charge writing was performed with the "dot" method shown in Fig. 3.3(a).

The quality of the topography image (Fig. 3.23(a)) is not as good as in air but the charge pattern could be imaged without problems (Fig. 3.23(b)). Typical artifacts can be seen in the KFM image at the borders and below the letter "T". It is not clear whether they come from contaminations, as one can partly see
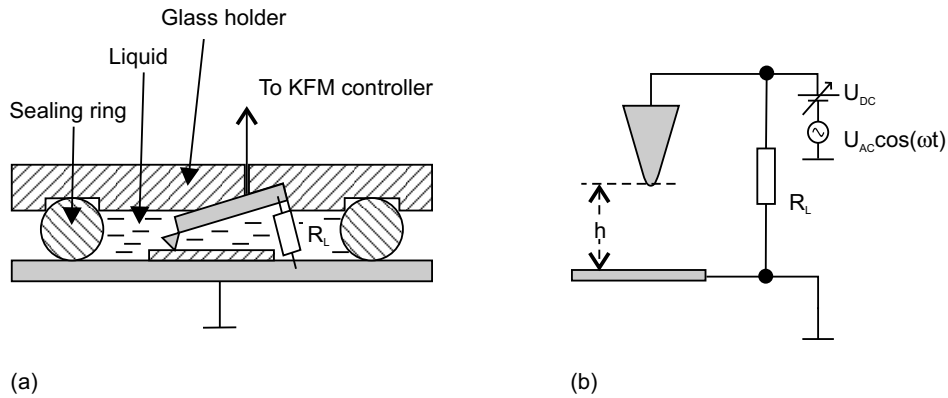
Figure 3.22: **AFM liquid cell.** The mounting of the liquid cell is shown in (a): The cantilever chip is fixed mechanically to a glass holder with an electrical connection to the KFM controller. A rubber sealing ring is clamped between the holder and the sample chuck. The resistance R_L, which depends on the electrical resistivity of the liquid and of geometrical factors, describes the short circuit between cantilever and sample or substrate. The equivalent circuit diagram is shown in (b).
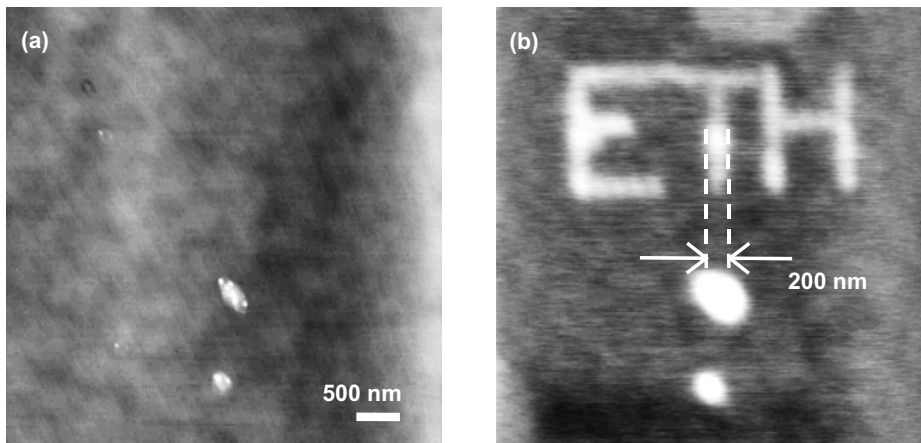
Figure 3.23: **Charge writing "ETH" symbol in PFD.** Positive charge "dots" written into a 30-nm-thick FC layer on Si substrate. Topography (a), z-range 10 nm, KFM signal (b), range 0.5 V, $U_p = +25$ V, $t_p = 10$ μs. The sample was immersed in PFD during writing and scanning.

features also in (a), or whether they are caused by vagabonding, electrostatic charges, which are often encountered in very dry, i.e. insulating, environments.

The charge decay in PFD is shown in Fig. 3.24. The method was the same as described in Sec. 3.3.6. The decay of the KFM signal is faster than in air and after about 30 min no charge could be detected anymore. In this dry environment it is likely that constantly generated counterions are transported to the surface charge pattern, which is thereby neutralised. These results imply that the particle

Figure 3.24: **Charge decay in PFD.** KFM signal, U_{DC}, vs. t, sample: 40-nm-thick FC layer on Si substrate immersed in PFD during charge writing and imaging, $U_p = \pm 25$ V, $t_p = 10$ μs.

attachment in this liquid must function on a timescale of about half an hour.

Chapter 4

Particle attachment

The experiments of the previous chapter (Sec. 3.4.2) have shown that water cannot be used as particle solvent because of its high conductivity leading to charge loss. Although electrodeposition of particles from aqueous suspensi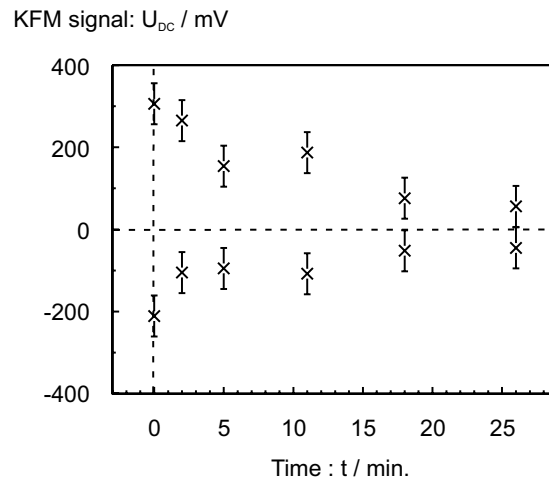ons is a well-known technique [VanderBiest99], its principles cannot be transferred directly. In electrodeposition a constant voltage is applied between two electrodes thereby leading to a constant electric field acting on the particles to be deposited. In the method presented here, nonpolar liquids of low conductivity such as hydroalkanes or perfluoroalkanes must be used to avoid charge decay and therefore decay of electric fields.

The deposition of carbon black particles to charged PTFE-foils has already been performed in the 70's by Feder reporting a resolution of the created particle structures of about 20 μm [Feder76]. The foils were electrified by electron beam charging and the carbon black was applied to the foils in form of a dry powder. Feder also reported deposition with increased structure quality using carbon black particles suspended in an insulating liquid not further specified.

The deposition of suspended 5-μm-silica beads from a fluorocarbon solvent to negative patterns generated by electron beam charge carrier injection into $CaTiO_3$-substrates was performed by Kobayashi et al. [Kobayashi98] and Fudouzi et al. [Fudouzi97]. They reported a resolution of about 21 μm for the line width of the charge patterns as determined by voltage contrast imaging with an electron microscope prior to immersion. The size of the deposited particle structures was of the same order of magnitude.

This chapter consists of 6 sections. First some preliminary considerations concerning the requirements for particle attachment, the colloidal aspects and the electrokinetics and triboelectricity in suspensions are discussed (Sec. 4.1). In Sec. 4.2 the experimental details are described. In Sec. 4.3 the results of the particle attachment are shown for silica as a demonstration material. In Sec. 4.4 the method is extended to nanometre-sized gold particles for showing the sub-

micrometre resolution that could be achieved. In Sec. 4.5 results of electrophoretic measurements of the particle charges are presented. Finally the results are shortly summarised and discussed in Sec. 4.6.

4.1 Preliminary considerations

4.1.1 Requirements for particle attachment

Three general conditions must be met for particle attachment:

- The charge pattern must be sufficiently stable during the time of the sample immersion.

- The suspension must be (meta)stable at least for the time of the sample immersion.

- The particles must carry a net, electric charge or must be polarisable so that the attractive force is strong enough to deposit a sufficient amount of particles on the patterns.

The first condition is best met by using the highly insulating liquids PFD or FC-77 as suggested from the results obtained in Sec. 3.4.2. Although silica or gold nanoparticle dispersions are not stable in perfluorocarbons a metastable suspension prepared by ultrasonication can always be used because, as will be shown, the attachment takes place on a relatively short time scale of the order of 10 min. The usual methods for adjusting the particle charge by variation of pH or of the electrolyte concentration cannot be applied in nonpolar liquids. Triboelectric charging of particles in insulating liquids shows a way out of this problem (Sec. 4.1.5).

In practice there are further requirements. As it can be seen directly from the formula for the electric field, $\vec{E}$, of a given surface charge, q_S,

$$\vec{E}(\vec{r}) = \frac{q_S}{4\pi\epsilon_0\epsilon_s r^2}\frac{\vec{r}}{r} \qquad (4.1)$$

the electric field of the charge patterns is less attenuated when using solvents of low dielectric constant, ϵ_s. Furthermore, the meniscus of an evaporating solvent can carry away the once deposited particles due to strong capillary forces. PFD as well as FC-77 are both liquids of low dielectric constant and of low surface tension (App. B.5.2). They are chemically inert and show a very low affinity for water uptake or organic contaminations. FC-77 has been used for the attachment because of its higher vapour pressure allowing a rapid evaporation of the solvent and because of its low viscosity leading to a higher mobility of the particles and thereby to a faster attachment process.

4.1.2 Diffusion

One of the most important physical quantities characterising suspensions is the diffusion coefficient, D, which is for spherical particles of radius R (Stokes-Einstein relation),

$$D = \frac{k_B T}{6\pi\eta R}, \tag{4.2}$$

in a solvent of dynamic viscosity η. The diffusion coefficient describes the magnitude of the flux of particles, $\vec{J}$, due to concentration gradients as described by Fick's 1st law, $\vec{J} = -D\nabla c$. For the particles used in this work, D varies from

$$D = 1.6 \cdot 10^{-11} \text{ m}^2/\text{s} \quad \text{for } R = 10 \text{ nm}$$
$$\text{to} \quad D = 2.1 \cdot 10^{-13} \text{ m}^2/\text{s} \quad \text{for } R = 750 \text{ nm}$$

in FC-77 at room temperature. As D describes how fast particles diffuse due to Brownian motion one can see from Eq. 4.2 that the particles move faster with decreasing size, a fact that is important for the deposition time. The average distance that a particle covers in the time t is $r_t := \sqrt{<r^2>} = \sqrt{6Dt}$ ([Hiemenz97], p.94). Thus, the particles diffuse, within 1 second, over a distance of

$$r = 1 \ \mu\text{m} - 10 \ \mu\text{m}.$$

4.1.3 Coagulation kinetics

A quantitative estimation of the coagulation kinetics can be made for determining the time frame within which the particle attachment must take place. The rapid coagulation regime applies to noninteracting particles, which move around due to random Brownian motion and which do not interact except on contact, where every collision of two units leads to the formation of a single unit. From this theory ([Myers99], p. 240) the half-life time for the particle number concentration can be calculated to

$$t_{1/2} = \frac{1}{8\pi R D c_0} \tag{4.3}$$

for monodisperse, hard spheres of radius R, diffusion constant D and initial number concentration c_0. With Eq. 4.2, one gets

$$t_{1/2} = \frac{3\eta}{4k_B T c_0}. \tag{4.4}$$

The concentration, c_0, of the diluted suspensions used in this work varies approximately between 10^8 and 10^{11} ml^{-1} as estimated from the preparation method and the quantities used. With the dynamic viscosity of FC-77, $\eta = 1.4 \cdot 10^{-3}$Ns/m^2, the half-life time is in the range of

$$t_{1/2} = 2.5 \text{ s} - 42 \text{ min}$$

at room temperature. These values are calculated taking into account only the viscosity of the solvent and the concentration but not the particle size or the van-der-Waals attraction respectively a possible repulsion due to electrical particle charges. In practice, $t_{1/2}$ is longer because the effective viscosity increases when the particles approach each other as the solvent has to be moved out of the way between the particles ([Myers99], p.241).

4.1.4 Electrokinetic forces

In a stationary solvent, without any electroosmotic flow, there are two contributions to forces acting on dispersed particles to which a static electric field, $\vec{E}$, is applied (Fig. 4.1).
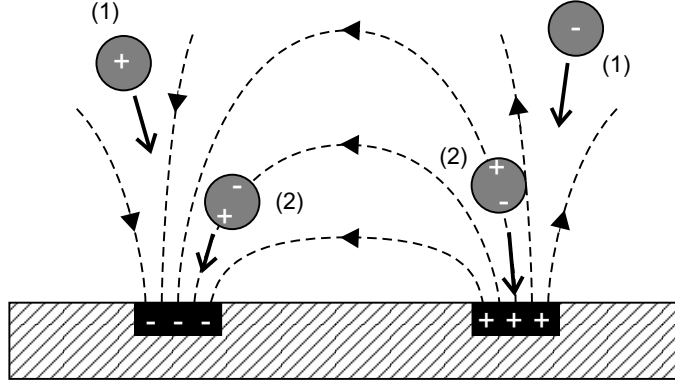
Figure 4.1: **Attraction of particles by inhomogeneous electric fields.** The dashed lines describe the electric field in the vicinity of the charge patterns. Particles carrying a net charge (1) are attracted by the Coulomb force towards the charge patterns of opposite polarity. Neutral but polarisable particles (2) with $\epsilon_p > \epsilon_s$ are attracted by the field gradient towards both patterns independently of the polarity.

1. In homogeneous as well as in inhomogeneous fields the Coulomb force

$$\vec{F}_{Coul} = Q\vec{E} \tag{4.5}$$

acts on particles carrying a net electric charge, Q. This force drives positively charged particles in and negatively charged particles oppositely to the direction of the electric field. For a given Q this force is independent of the materials of particle and solvent.

2. In inhomogeneous fields the dielectrophoretic (gradient or polarisation) force

$$\vec{F}_{Diel} = 2\pi R^3 \frac{\epsilon_p - \epsilon_s}{\epsilon_p + \epsilon_s}\epsilon_0\epsilon_s\nabla E^2 \tag{4.6}$$

44

acts on polarisable particles of radius R independently of their net charge, the dielectric constants of particle and solvent being ϵ_p and ϵ_s respectively [Jones95]. The particles are driven in the direction of the field gradient for $\epsilon_p > \epsilon_s$ and oppositely to the direction of the field gradient for $\epsilon_p < \epsilon_s$.

Both forces are of the same order of magnitude and, in practice, the electrokinetic movement is additionally superposed by sedimentation and forces due to liquid flow such as electroosmosis, convection and Brownian motion.

4.1.5 Coehn's rule

Coehn's rule about triboelectric contact charging of insulators states that [Coehn09] *if two dielectric materials are brought into contact the one with the higher dielectric constant is charged positively against the one with the lower dielectric constant and the arising potential difference is proportional to the difference of the dielectric constants of the materials.*

Coehn and Raydt framed this rule on the basis of numerous experiments investigating the electroosmotic rise of different liquids in glass, quartz as well as diamond capillaries and, in a hypothesis, attributed the results to electron transfer between the materials as they were able to exclude some straightforward interpretations such as the dissociating force of a liquid of higher ϵ_r and uneven distribution of ions between the materials in contact [Coehn09].

Although the rule is quite old and its exceptionally good observation is striking, a microscopic, i.e. an "electronic", theory has not yet been established [Castle97]. Triboelectrification, on the other hand, is known for a long time and a large body of literature is available. The "surface state theory" describing the electronic behaviour of contacted dielectrics is generally accepted. It states that a pseudo- or effective surface work function exists for electrons in insulators, which applies to energetic states within the wide band gap but localised at the surface [Castle97]. However, this theory does not provide a link between the surface work function and the dielectric constant.

4.2 Experimental details

4.2.1 Large-pattern generation

The generation of charge patterns of lateral sizes ≥ 40 μm (Fig. 4.2) was performed as follows:

1. The AFM tip was disconnected from the KFM controller and connected to the pulse generator.

45

2. The normal scanning operation of the AFM was turned on with tapping mode z-feedback enabled at a scan size corresponding to the lateral size of the desired structure.

3. When the tip reached one corner of the desired structure the pulse sequence was activated at a pulse frequency of 50 Hz for given U_p and t_p, thereby producing a large number of charge dots during the continuing lateral motion of the AFM tip. The areal "density" of the charge dots was determined by the tip velocity, $v_T = 2 \cdot scansize \cdot scanrate$, and the number, n_S, of scan lines per image (128, 256 or 512).

4. Reaching the opposite corner the pulse sequence was stopped and the procedure was repeated as desired (for example the scan angle was rotated by 90° to generate cross-shaped structures).
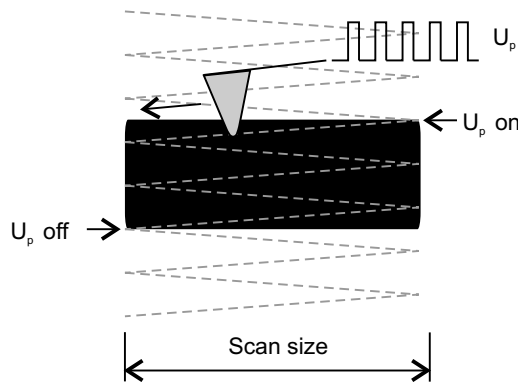
Figure 4.2: **Charge writing of large patterns.** Electrified area in black. The tip draws its zic-zac-motion (pitch of the fast scan lines exaggerated) during normal scanning in tapping mode. The pulse voltage is turned on and off at the positions indicated by $U_p$on and $U_p$off respectively. The scan size determines the size of the pattern.

4.2.2 Preparation of suspensions

The attachment of particles has been carried out using monodisperse, commercial silica particles (1.5-μm-diameter and 290-nm-diameter microspheres, Bangs Laboratories Inc., Fishers IN, USA, and 50-nm-diameter SiO_2 microspheres, Polysciences Inc., Warrington PA, USA) as well as gold particles (21-nm-diameter colloidal gold, Sigma-Aldrich Corp., St. Louis MO, USA). Silica and gold were chosen as dielectric and conductive materials respectively and are available as aqueous suspensions of different concentrations except for the 1.5-μm-diameter beads, which are provided as dry powder.

The fluorocarbon suspensions are prepared by two different methods using an ultrasonic bath (B1210E, BRANSON ULTRASONICS CORP., Danbury, CT, USA):

- Adding dry (or vacuum-dried) powder to the fluorocarbon liquid and subsequent ultrasonication.

- Pipetting a small amount of the undiluted, aqueous particle suspension onto a larger volume of FC-77 in a small dish (Fig. 4.3) and subsequent ultrasonication.

After stopping the ultrasonication the sample was immediately immersed in the FC-77.
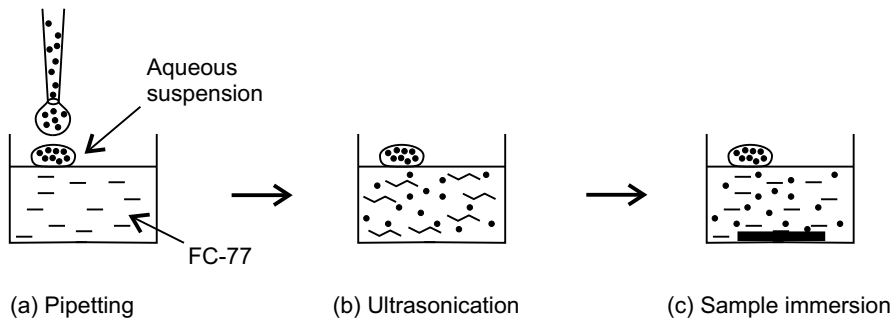
Figure 4.3: **Charge pattern development.** A small amount of the aqueous particle suspension is pipetted onto a larger amount of the non-water-miscible FC-77 (a). Ultrasonication is applied for several minutes (b) and after stopping the ultrasonication the electrified sample is immediately immersed in the FC-77 avoiding contact of the sample with the remaining water droplet (c).

4.3 Results of silica particle attachment

4.3.1 1.5-μm-diameter beads

Fig. 4.4 shows light microscopy (LM) images of silica particles of 1.5 μm diameter deposited on a 150-μm-large, negative, cross-shaped pattern. Positive patterns did not lead to any attachment. The suspension was prepared by ultrasonical dispersion of the dry powder in FC-77. Although most of the particles are deposited on the pattern the structure definition is not very good. The typical chaining effect of dispersed, dielectric microspheres can be seen in Fig. 4.4(a). The beads were probably aligned to the electric field lines and fell down to the surface after solvent evaporation. Furthermore, the deposition is not uniform showing partly
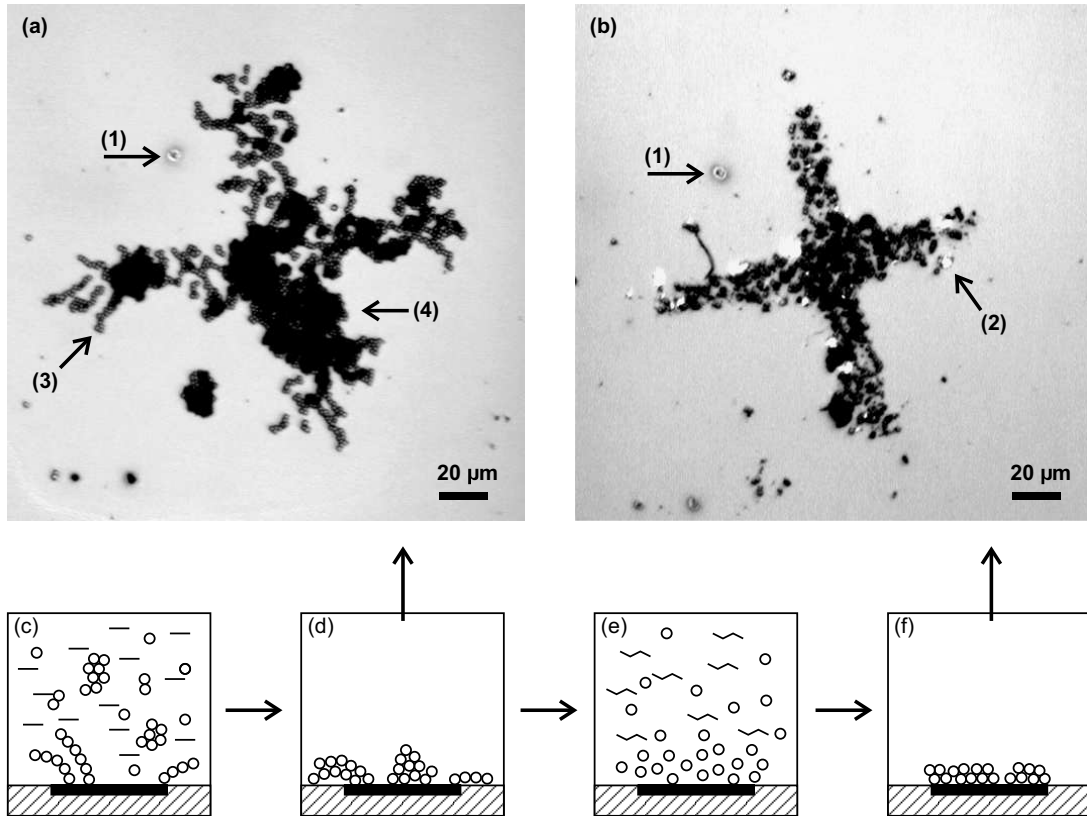
Figure 4.4: **1.5-μm-silica particles.** Reflection contrast LM images ($20\times$, 0.5 NA) of 1.5-μm-diameter silica particles deposited on a 150-μm-cross-shaped pattern (a) and (b). *Sample:* 150 nm FC layer on Si ($\rho = 0.1$ Ωcm), $U_p = -60$ V, $t_p = 1$ ms, $v_T = 50$ μm/s. *Suspension:* Dry silica particles ultrasonically dispersed in FC-77, injected directly into the liquid cell (a few min immersion until evaporation of the liquid), (a) directly after evaporation, (b) sample re-immersed in pure FC-77 + ultrasonication for 5 min.
Labels: (1) defect of the FC film as reference for the orientation of the two images, (2) film defect caused by the application of ultrasonic energy, (3) chains, (4) agglomerates.
Outline of multiple immersion: The particles agglomerate in the undisturbed solvent and form chains (c), after drying, agglomerates are formed on the surface (d), repeated ultrasonication in pure solvent breaks up the agglomerates but the particles are staying close to the charge pattern and can rearrange (e), after drying, the structure definition is better and the size of the agglomerates as well as of the chains are reduced (f).

large chunks as well as voids. These effects, which are due to the poor solvability of the particles, were always observed for dry-dispersed powders.

Immersing the sample in pure FC-77 a second time and applying ultrasonication increased the pattern definition due to the break up of agglomerates and chains and led to a better distribution of the particles on the pattern (b). However, long ultrasonication can damage the FC layers so that cracks and pieces (2) torn out of the film could be observed.

The particles could be visually observed by LM with an objective of large working distance during the attachment process. For comparison with the visual observation one can make an estimate of the force $F = QE$ acting on the silica beads and their kinetics in the vicinity of the charge pattern. Therefore, the electric field of a cross-shaped pattern is approximated by the field of a charged, circular disc of the same area as the cross with the same surface charge density, σ. The area of the cross with beam length 150 μm and arm width 20 μm is 5600 μm^2 (Fig. 4.5(a)). The radius of the equivalent disc is then $r_{disc} = 42$ μm
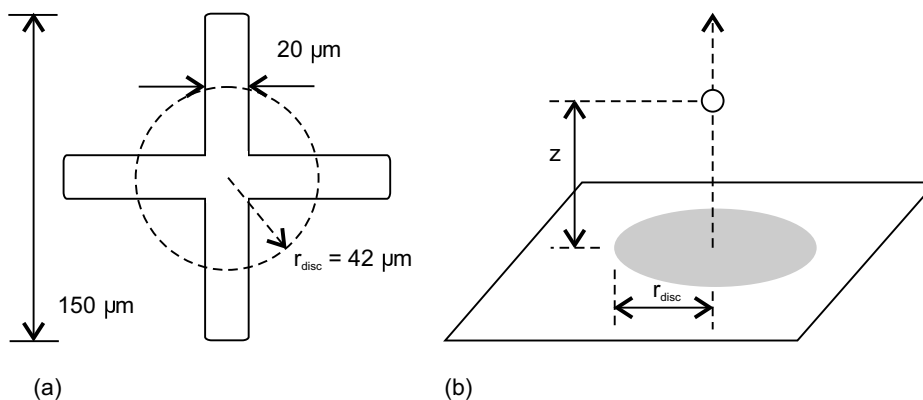
Figure 4.5: **Estimation of the electric field.** 150-μm-sized cross pattern approximated by a circular disc of the same area (a). Calculation of the electric field at distance z above the disc (b).

and the calculation is performed for a point on the disc axis at distance z from the disc (Fig. 4.5(b)). The electric field is

$$E(z) = \frac{\sigma}{2\epsilon_0\epsilon_s} \left(1 + \frac{z}{\sqrt{r_{disc}^2 + z^2}} \right) \tag{4.7}$$

with the dielectric constant of the solvent ϵ_s. By inserting $\sigma = 2000$ EC/μm^2, as a typical value obtained in Sec. 3.3.3, and $\epsilon_s = 1.86$ into Eq. 4.7 one obtains for the force acting on a single particle, which carries 10 elementary charges (see also Sec. 4.5) at distance $z = 150$ μm

$$F_{Coul} = 30 \cdot 10^{-12} \text{ N}.$$

Thus, the force acting on the particles is typically in the pN-range and with Stokes' law, $F_S = 6\pi\eta R v$, for the drag force one can make an additional estimation for the particle velocity, v, at stationary conditions with $F_S = F_{Coul}$ leading to

$$v \approx 1.5 \text{ mm/s}$$

with $\eta = 1.4 \cdot 10^{-3}$ Ns/m^2 and $R = 0.75$ μm. This value is only an estimation under special assumptions but it gives a good idea of the particle kinetics during the attachment.

4.3.2 290-nm-diameter particles

The polarity of the particle charge as well as the influence of the preparation were investigated using 290-nm-diameter particles. Fig. 4.6 shows the attachment to a cross-shaped charge pattern of a size of 40 μm. One negative (a) as well as one positive (b) charge pattern were written close to each other. Fig. 4.6(c) shows a reflection contrast LM image after immersion and evaporation of the remaining liquid.

The particles clearly adhere only to the negative pattern whereas the positive pattern is nearly free of particles. There are particles, which are unspecifically deposited around the patterns. Rinsing with pure FC-77 or with UHQ water after deposition, removed a few of the unspecifically deposited particles but the cross structures were not affected. Immersing the samples into pure FC-77 and applying additional ultrasonication, removed most of the particles and destroyed the structures if the samples were directly taken out of the ultrasonically agitated liquid. If the samples were ultrasonicated in pure FC-77 for a few minutes and then left in the liquid for several minutes without ultrasonication a "reconstruction" of the structures could be observed as described in Sec. 4.3.1. Immersing the samples into UHQ water and applying additional ultrasonication removed almost all particles and destroyed the structures.

Although these rinsing tests could provide only qualitative statements about the strength of the particle adhesion force the tendency could be found that the drag force and the turbulences acting on the particles during rinsing are not strong enough to remove them. On the other hand, the silica particles could be easily pushed away by the AFM tip when trying to image them in tapping mode. This has not been observed with 20-nm-gold particles (Sec. 4.4).

Fig. 4.7 shows an LM image of deposited particles which were vacuum-dried prior to ultrasonical dispersion in FC-77. The structure definition is poorer than for the suspension prepared from the aqueous solvent as described in Sec. 4.2.2. Although the particles are attracted by the charge pattern they are still agglomerated to large chunks and do not cover well the surface. This behaviour could
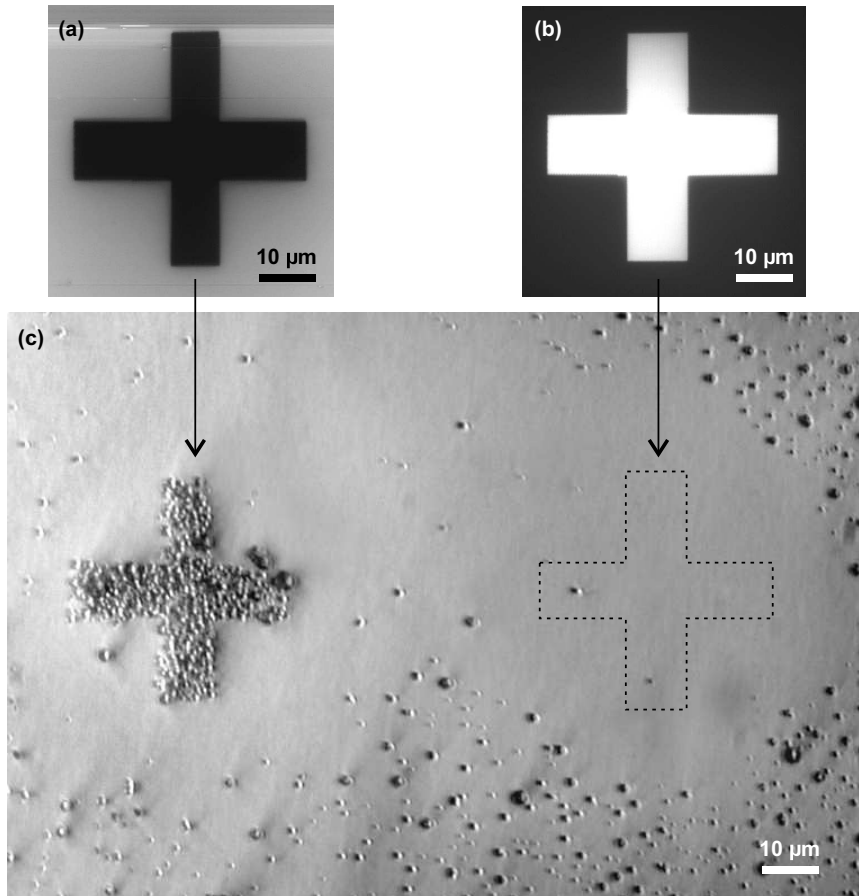
Figure 4.6: **Attachment of 290-nm-silica particles.** KFM images (a) and (b) recorded prior to sample immersion with KFM signal range 3 V; the zero-potential values are different in (a) and (b). Reflection contrast LM image (40×, 0.75 NA) after immersion in FC-77 and evaporation of the solvent (c). Sample: 80 nm FC layer on Si ($\rho = 0.1$ Ωcm), $U_p = -60$ V (a) and $U_p = +60$ V (b), $t_p = 1$ ms, $v_T = 24$ μm/s. Suspension: Ultrasonically dispersed mixture of 50 μl (10-wt.-%) silica sol + 10 ml FC-77, $t_D = 51$ min. The arrows indicate the locations of the respective charge patterns. The dashed lines in (c) indicate the position of the positive charge pattern. A shutter was partially introduced into the optical path of the LM to enhance the contrast of the silica particles.

be observed in all experiments with vacuum-dried silica particles smaller than 1.5-μm-beads. The particles attached to the negative patterns but the structure quality has always been worse than with the suspensions prepared by the method shown in Fig. 4.3.

51
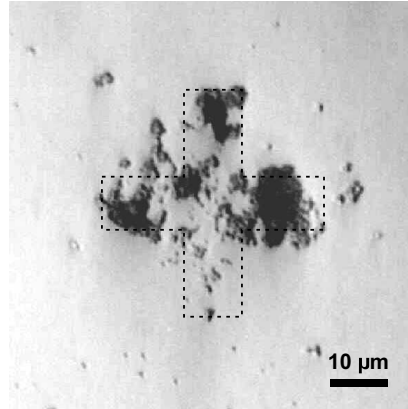
Figure 4.7: **Structure quality.** Reflection contrast LM image (40×, 0.75 NA) of 290-nm-diameter silica particles deposited on cross pattern. Sample: 80 nm FC layer on Si ($\rho = 0.1$ Ωcm), $U_p = -60$ V, $t_p = 1$ ms, $v_T = 24$ μm/s. Suspension: 50 μl (10-wt.-%) silica sol vacuum-dried (3 min at $4 \cdot 10^{-4}$ hPa) prior to ultrasonical dispersion in 5 ml FC-77, $t_D = 28$ min. The dashed lines indicate the position of the charge pattern.

4.3.3 50-nm-diameter particles

For investigating the resolution of the method, particles of 50 nm diameter were deposited onto a grid line pattern written as described in Sec. 3.2.1 (Fig. 3.3(b)). The line length was ≈ 20 μm, the line width was 650 nm (FWHM) and the line pitch increased from left to right from 800 nm to about 1.5 μm, respectively. Fig. 4.8 shows the KFM image of the charge pattern recorded prior to sample
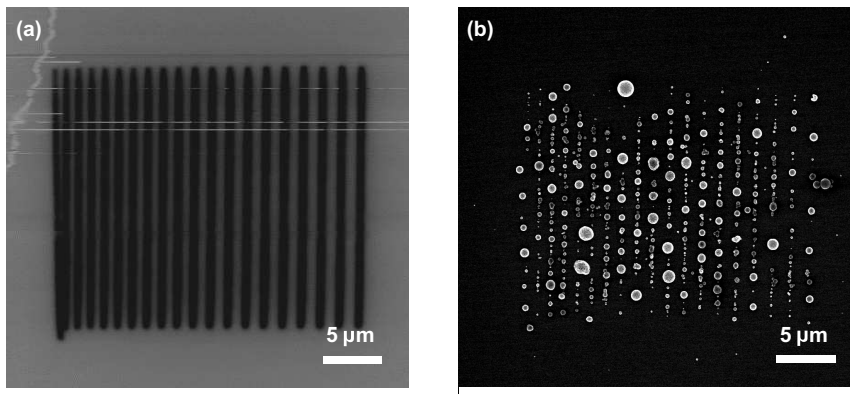
Figure 4.8: **Attachment of 50-nm-silica particles.** KFM signal image (a),(signal range 3 V) recorded prior to sample immersion in FC-77 and scanning electron microscopy image (b) after immersion, evaporation of the solvent and metallisation of 5 nm Pt. Sample: 90 nm FC layer on Si ($\rho = 0.1$ Ωcm), $U_p = -60$ V, $t_p = 1$ ms, $v_T = 10$ μm/s. Suspension: 380 μl (5.34-wt.-%) silica sol + 5 ml FC-77, $t_D = 2$ min. Acceleration voltage in (b) 30 kV.

immersion (a) and an electron microscopy image after particle attachment, evaporation of the solvent and metallisation (b). The 50-nm-particles attached only to the negative pattern. Fig. 4.8(b) shows that the lines were not continuous and that the particles partly formed agglomerates of up to 1 μm diameter. Image zooms reveal the almost spherical, raspberry-like aggregates formed by the particles (Fig. 4.9). The resolution in terms of the possibility of distinguishing
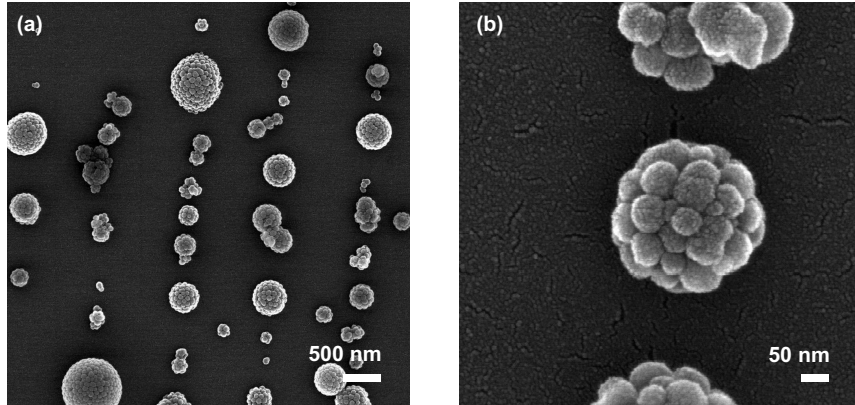
Figure 4.9: **Agglomeration of silica particles.** Zoomed electron microscopy images of the sample shown in Fig. 4.8. The orientation of the grid lines is vertical.

separate lines is about 1 μm.

4.4 Results of gold particle attachment

An extension of the method to metal nanoparticles is shown in Fig. 4.10. An FC-77 suspension of 20-nm-diameter gold particles prepared as described in Fig. 4.3 was used for the attachment onto 4 negative charge lines of 40 to 50 μm length and ca. 500 nm width (FWHM). Similar patterns with positive lines on the same sample did not lead to any particle attachment.

The gold particles are difficult to resolve laterally by AFM because the tip radius is of the same order as the particle diameter. The line width was about 500 nm. A zoom shows that the lines are not continuous and some of the particles are probably agglomerated to each other (Fig. 4.10(b)).

Fig. 4.11 shows the topography (a) and the KFM signal (b) of attached 20-nm-diameter gold particles on a 40-μm-sized cross, thereby exhibiting directly the deposition of the particles on the negative pattern. After 5 min sample immersion the charge pattern could still be detected by KFM (black areas). The deposited particles show a positive KFM signal but it cannot be stated definitely whether this is due to a remaining positive charge of the gold or whether it is caused by
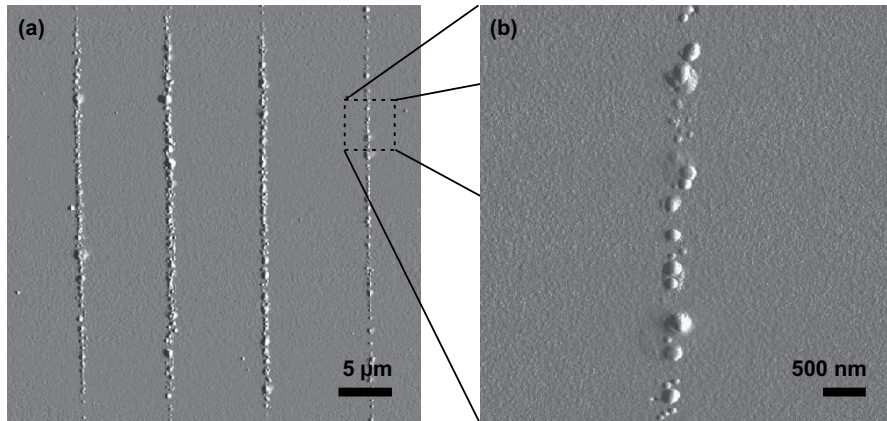
Figure 4.10: **Attachment of 20-nm-gold particles.** Tapping Mode AFM images of gold particles after immersion and evaporation of the solvent, amplitude signal range arbitrary. Sample: 100 nm FC layer on Si ($\rho = 0.1$ Ωcm), $U_p = -60$ V, $t_p = 1$ ms, $v_T = 10$ μm/s. Suspension: Ultrasonically dispersed mixture of 400 μl Au sol ($c = 5 \cdot 10^{11}$ml^{-1}) + 7 ml FC-77, $t_D = 10$ min.
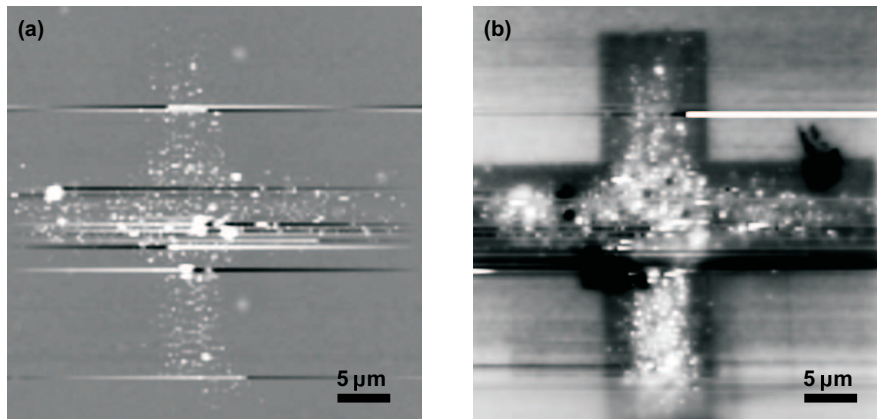
Figure 4.11: **Crosswise attachment of 20-nm-gold particles.** Tapping Mode AFM images of gold particles after immersion and evaporation of the solvent, topography (a) range 500 nm and KFM signal (b) with range 3 V. Sample: 130 nm FC layer on Si ($\rho = 0.1$ Ωcm), $U_p = -60$ V, $t_p = 1$ ms, $v_T = 24$ μm/s. Suspension: Ultrasonically dispersed mixture of 500 μl Au sol ($c = 5 \cdot 10^{11}$ml^{-1}) + 5 ml FC-77, $t_D = 5$ min.

the material contrast or corrugations leading to topographic artifacts of the KFM signal.

4.5 Electrophoretic determination of the particle charge

All particles used in Secs. 4.3 and 4.4 attach only at negative but not at positive charge patterns. Thus, it can be inferred that the particles carry a positive net charge and are attracted by Coulomb force. For particles of a size larger than the wavelength of light their charge, Q, can be determined by direct LM observation of the electrophoretic mobility in an externally applied, electric field, E, in a Millikan-like setup. In the stationary case a particle carrying the charge Q travels at constant velocity v and the Coulomb force is equal to Stokes drag force

$$F_S = F_{Coul}. \tag{4.8}$$

For spherical particles of radius R the Stokes drag force in a medium of dynamic viscosity η is

$$F_S = 6\pi\eta v R. \tag{4.9}$$

With Eq. 4.5 and Eq. 4.9, Eq. 4.8 can then be written as

$$Q = \frac{6\pi\eta v R s}{U} \tag{4.10}$$

with $E = U/s$ and the voltage U applied to parallel plate electrodes separated by the distance s. The surface charge density is then

$$\sigma = \frac{Q}{4\pi R^2} = \frac{3\eta v s}{2UR}. \tag{4.11}$$

The experimental setup of the electrophoretic measurement is shown in Fig. 4.12. For determination of v, the trajectories of the colloid particles were observed by LM using a 10× objective in transmission contrast. The LM was equipped with a digital camera (CCD camera 4912-5000, COHU INC., San Diego CA, USA). A frame grabber card (LG3, SCION CORP., Frederick MD, USA) as well as a SW imaging system (SCION IMAGE SW 1.62C, NATIONAL INSTITUTES OF HEALTH, Bethesda MD, USA) were used for recording movies of up to 10 s length with a frame rate of 12.5 Hz. The liquid cell consisted of a transparent vessel made of poly(dimethylsiloxane) rubber, which was open only at the top side and could be covered by a cover slip.

The electric field was generated by applying a voltage of $U = 66$ V to the parallel electrodes immersed in the cell in a vertical arrangement, i.e. the field lines are horizontal (Fig. 4.12(b)). The distance of the electrode plates was fixed by teflon spacers to $s = 510$ μm ± 50 μm leading to an electric field strength of

$$E = U/s = 1300 \text{ V/cm} \pm 130 \text{ V/cm},$$
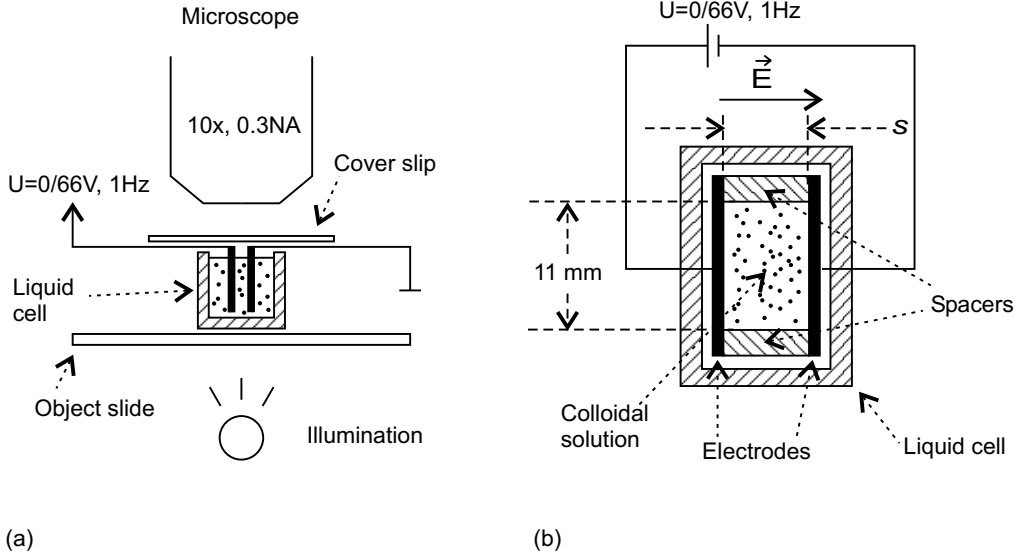
Figure 4.12: **Electrophoretic measurement.** Side view (a) and top view (b), both not to scale. The liquid cell supported by an object slide is filled with the suspension/emulsion, which is observed by LM (10×, 0.3 NA) in transmission contrast (a). The electrodes, to which a square wave voltage of 66 V amplitude and 1 Hz frequency is applied, are separated by teflon spacers (b) at a distance $s = 510 \ \mu m \pm 50 \ \mu m$.

which is much lower than the breakdown voltage of fluorocarbon fluids being usually of the order of 100 kV/cm. The lateral dimensions of the plates are 3 mm × 15 mm and the observation was performed at a sufficient distance from the edges of the plates by choosing an appropriate focus plane so that the electric field can be assumed to be homogeneous.

The electrophoretic motion of particles in liquids, $\vec{v}_{el}$, is always superposed by collective drifts of particles together with the liquid due to convection flows, $\vec{v}_{flow}$, so that the measured particle velocity is

$$\vec{v} = \vec{v}_{el} + \vec{v}_{flow}. \tag{4.12}$$

To distinguish $\vec{v}_{el}$ from $\vec{v}_{flow}$ all measurements have been performed by applying an alternating (square wave) voltage between 0 and +66 V with frequency 1 Hz and duty cycle 0.5 so that the field is present only for 0.5 s followed by a period of 0.5 s without field. Assuming that the thermal situation in the cell does not change significantly within one second, $\vec{v}(E = 0) = \vec{v}_{flow}$ has been subtracted from $\vec{v}(E \neq 0)$ for each cycle and for each particle so that $\vec{v}_{el}$ was obtained.

The experiments were performed using PFD instead of FC-77 as solvent because the latter shows too much convection flow for a good particle tracking by LM. The viscosity of PFD is about 3.5× higher than that of FC-77 but the dielectric constants of both liquids are the same ($\epsilon_r = 1.86$) so that according to

Coehn's rule the triboelectrically generated particle charge should be the same (Sec. 4.1.5).

Electroosmotic solvent flow along the cell walls can be neglected in this setup because the nonpolar solvent PFD does not contain hydrated ions and because the measurement has been performed at sufficient distance from the cell walls.

The electrophoretic mobility of SiO_2 particles with 1.5 μm diameter has been compared with that of UHQ-water droplets ultrasonically dispersed in PFD. The silica suspension was prepared as described in Sec. 4.2.2 by dispersing dry powder in PFD. The water/PFD emulsion was prepared by ultrasonication of a few μl UHQ-water added to 1 ml PFD.

As tribocharging is a statistical process especially on small scales a statistical evaluation of the trajectories of at least 20 particles has been performed and for each particle several cell voltage cycles have been averaged for calculating the charge, Q, with Eq. 4.10 and the surface charge density, σ, with Eq. 4.11 from the measured particle velocity, v. Due to their small mass the particles followed the electric field quasi instantaneously.

As one can see from Eqs. 4.10 and 4.11 the particle radius, R, must be known for the calculation. In the case of silica beads R is a known quantity. However, when a suspension is ultrasonically produced in nonpolar solvents a large part of the colloidal particles are agglomerated to larger units. A separate LM measurement (40$\times$, 0.75 NA) of the size distribution of the agglomerates is shown in Fig. 4.13. On average the silica spheres are agglomerated to units of 2 ± 1.85
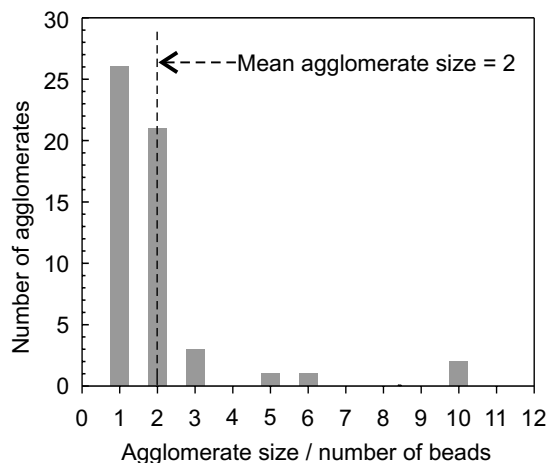

Figure 4.13: **Size distribution of silica particle agglomerates.** 1.5-μm-diameter silica beads ultrasonically dispersed in PFD and subsequently analysed by LM. Abscissa = size of the agglomerate, ordinate = number of agglomerates.

beads. Although the formula for Stokes drag force (Eq. 4.9) is not strictly valid

for non-spherical bodies it is taken here as an approximation by calculating with a mean radius of $R = 2 \cdot 0.75 \ \mu$m.

In the case of ultrasonically dispersed water droplets the radii show a normal distribution with average value

$$R = 0.59 \ \mu\text{m} \pm 0.19 \ \mu\text{m},$$

which has also been determined by a separate LM measurement ($40\times$, 0.75 NA).

Tab. 4.1 shows the results of the electrophoretic measurements for SiO_2 particles and water droplets in comparison. The velocity, v, of the silica as well

	R/μm	$v/(\mu\text{m/s})$	Q/EC	$\sigma/(\text{EC}/\mu\text{m}^2)$
SiO_2	1.50 ± 1.39	4.67 ± 1.91	33 ± 48	1.18 ± 1.72
H_2O	0.59 ± 0.19	5.89 ± 0.94	16 ± 9	3.66 ± 2.05

Table 4.1: **Charge and surface charge densities of SiO_2-beads and H_2O-droplets.** $R =$ mean radius of SiO_2 agglomerates and of water droplets, respectively, $v =$ averaged, measured particle velocity, $Q =$ total particle charge, $\sigma =$ surface charge density (see text).

as of the water particles is of the order of a few μm/s, the total particle charge is of the order of only a few tens of EC leading to surface charge densities of $1.18 \ \text{EC}/\mu\text{m}^2 \pm 1.72 \ \text{EC}/\mu\text{m}^2$ for the silica beads and $3.66 \ \text{EC}/\mu\text{m}^2 \pm 2.05 \ \text{EC}/\mu\text{m}^2$ for the water droplets. In both cases some of the particles were charged oppositely to the majority of the particles, which is not surprising as only a small number of EC is exchanged. These statistical fluctuations lead to a standard deviation of the velocity measurements of 41 % and 32 % for silica particles and for water droplets, respectively. Together with the error caused by the agglomeration of silica beads and the uncertainty of s, a conservative estimation leads to the relatively large, total uncertainty of Q and σ (Tab. 4.1) especially for silica beads. Nevertheless, the average values of Q and σ are of reasonable magnitude and confirm the observations of Sec. 4.3 that the particles are positively charged. Furthermore, it can be shown that water droplets exhibit a $3\times$ higher charge than silica beads.

4.6 Summary and discussion

Independently of the preparation method, silica as well as gold particles attach only to the negative patterns and the resolution, i.e. the smallest feature size, which can be achieved, is about $20 - 25\times$ the particle size. The development time seems to decrease with decreasing particle size although further, quantitative investigations about the development times have not been carried out.

For dry silica particles dispersed in FC-77 the attraction is mainly due to the Coulomb force, $\vec{F}_{Coul}$, (Eq. 4.5). If the dielectrophoretic contribution, $\vec{F}_{Diel}$, (Eq. 4.6) to the total force was significant a certain amount of particles would have been deposited also on the positive areas due to the inhomogeneous fields generated by the charge patterns above the surface (Fig. 4.1). Thus, as the silica particles attach only to the negative patterns the particles are positively charged.

This behaviour can be explained by triboelectrification of the dielectric particles in contact with the dielectric solvent, the polarity being in agreement with Coehn's rule (Sec. 4.1.5) as the dielectric constants are

$$\epsilon_{SiO_2} = 3.7 > \epsilon_{FC-77} = 1.86.$$

The results obtained for the suspensions prepared by the method shown in Fig. 4.3 for silica as well as for gold particles suggest a similar explanation. As it can be seen in Fig. 4.9 the particles are agglomerated to mostly spherical aggregates, which are an indication of water layers remaining around the agglomerates and holding together the particles due to capillary forces. Control experiments performed by ultrasonication of pure water with FC-77 showed that small water droplets were transferred into the nonpolar solvent, as determined by LM, and led to the turbidity of the FC-77. One can infer that the hydrophilic particles are trapped within these water droplets and are thereby transferred into the nonpolar oil (Fig. 4.14). The energy necessary for creating the droplets, i.e. for
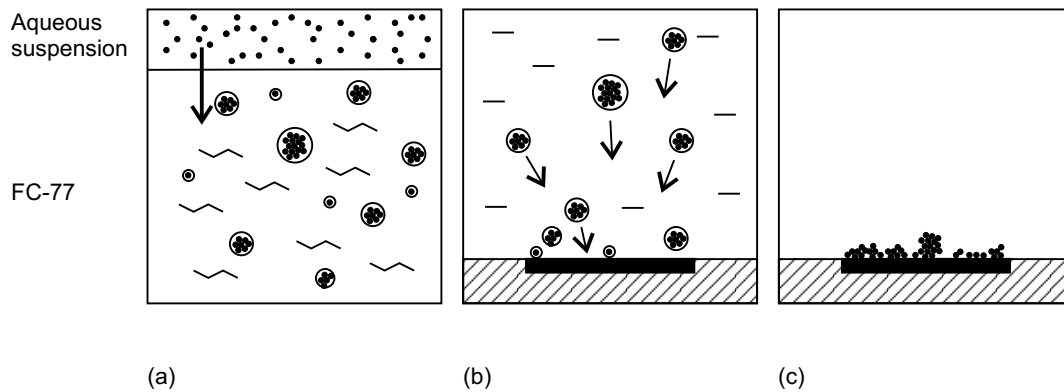
Figure 4.14: **Formation of water droplets.** Ultrasonication is applied to the water, which is in contact with the FC-77. Small water droplets containing the solid particles are generated by ultrasonication and transferred into the FC-77 (a). The positively charged water droplets are attracted towards the charge pattern (b). After evaporation of water and FC-77 the particles remain on the sample surface forming small aggregates (c).

increasing the water/FC-77 interfacial area, is provided by the ultrasonication. From Coehn's rule follows that the water droplets are also positively charged, as

experimentally confirmed by electrophoretic measurements (Sec. 4.5), because

$$\epsilon_{\text{H}_2\text{O}} = 81 > \epsilon_{\text{FC-77}} = 1.86.$$

Furthermore, the fact that $\epsilon_{\text{H}_2\text{O}} \gg \epsilon_{\text{SiO}_2}$ results in a higher charge of the droplets than of the solid beads leading to a stronger attraction by the charge patterns and thereby to a much better structure definition (for comparison see Fig. 4.6(c) and Fig. 4.7). Additionally, the higher charge increases the mutual repulsion of water droplets thereby preventing them to coagulate too fast.

According to the proportionality predicted by Coehn's rule the charge increase would be about

$$\frac{\epsilon_{\text{H}_2\text{O}}}{\epsilon_{\text{SiO}_2}} \approx 22$$

whereas the experimentally determined surface charge of water droplets is only about $3\times$ higher than that of silica beads (Sec. 4.5).

The reason for this discrepancy is not clear. On the one hand, the electrophoretic measurements exhibit a large statistical error and, on the other hand, questions remain open from the measurements of Coehn and Raydt [Coehn09]: their experiments have been performed only for the solid-liquid interface and it is not clear whether Coehn's rule can also be applied to the liquid-liquid interface. Another question is whether a dielectric-dielectric interface of a given area shows the same charge for different interfacial geometries such as, e.g., a planar interface or an interface being distributed over a large number of microscopic bodies.

The dielectrophoretic force, F_{Diel}, of water droplets in FC-77 is also higher than the one of silica particles but the increase is only about (Eq. 4.6)

$$F_{Diel,\text{H}_2\text{O}} : F_{Diel,\text{SiO}_2} = \frac{\epsilon_{\text{H}_2\text{O}} - \epsilon_{\text{FC-77}}}{\epsilon_{\text{H}_2\text{O}} + \epsilon_{\text{FC-77}}} : \frac{\epsilon_{\text{SiO}_2} - \epsilon_{\text{FC-77}}}{\epsilon_{\text{SiO}_2} + \epsilon_{\text{FC-77}}} \approx 2.9,$$

which is obviously not sufficient for permitting attachment to positive patterns.

Thus, the water droplets act as carriers for the solid particles and transport them to the charge patterns. This mechanism works for dielectric as well as for metallic particles. The spherical shape of the agglomerates shown in Fig. 4.9 indicates that the water droplets maintain their spherical shape upon attachment to the sample surface. This can be due to the strong hydrophobicity of the FC electret leading to a large contact angle of the deposited water droplets. Upon evaporation of the FC-77 as well as of the water, the solid particles (or agglomerates) stay on their positions and form the pattern structure (Fig. 4.14).

Chapter 5

Conclusions and outlook

In this work a method has been developed for electrostatically attaching colloidal particles to dielectric surfaces, which are locally electrified by a biased AFM tip. A two-step process was realised using silica and gold particles of different sizes suspended in an insulating liquid and deposited to PECVD-produced PTFE-like fluorocarbon thin-films on semiconductor and metal substrates.

In the first step, charge patterns were written with high resolution by applying voltage pulses to an AFM tip, which is scanned laterally in tapping mode under ambient conditions. Highly doped Si tips were used because they are more resistant against abrasion than metal coated tips. In the second step, the electrified samples were immersed in the suspensions and the charged nanoparticles were attracted by the oppositely charged surfaces and attached according to the geometric patterns.

KFM was used for investigating the charge storage properties of the fluorocarbon film. With a pulse generator coupled to the conductive AFM tip positive as well as negative charge dots of a size down to 100 nm were written – a limit, which is likely to be set rather by the imaging than by the charge writing method.

The patterns showed a very slow decay of the order of several hours even at very high humidities. No lateral spreading could be observed and the use of metal substrates did not strongly affect the charge leakage through the substrates. It turned out that the amount of injected charge increases with increasing pulse voltage and film thickness but shows no dependence on the pulse length if the cantilever tapping period is smaller than the pulse length. Direct charge measurements showed that amounts of ca. 1000 to 4000 elementary charges per voltage pulse are transferred.

Immersion of the electrified samples in UHQ water led to a rapid neutralisation of the charge patterns whereas for highly insulating perfluorocarbon oils the charge decay was significantly slower. Therefore, the nonpolar perfluoroalkane FC-77 was used as solvent for the particles. In PFD, a nonpolar fluorocarbon

oil similar to FC-77, charge writing as well as KFM imaging was possible. This can be used in the future for reducing the number of process steps by performing charge writing and particle attachment simultaneously without having to expose sensitive samples to the environment.

The suspensions were prepared by ultrasonically dispersing the silica and the gold particles in FC-77. The triboelectrically, positively charged particles attached to negative charge patterns by Coulomb attraction. According to Coehn's rule the positive charge of the SiO_2 particles could be attributed to their higher dielectric constant compared to the one of the solvent. An increased structure definition could be achieved by preparing the suspensions with additional water, forming tribo-charged droplets of increased surface charge. The droplets trapped the hydrophilic, solid particles inside and carried them to the charge patterns. With silica particles of 50 nm diameter and gold particles of 20 nm diameter, feature sizes of ca. 1 μm and 500 nm, respectively, could be achieved.

The suspensions used and the preparation method limit the resolution to about $25\times$ the particle size. Silica as well as gold particles are very lyophobic with respect to fluorocarbon oils and rapidly form agglomerates. The usual charge stabilisation methods for aqueous suspensions cannot be applied to nonpolar liquids and suitable surfactants for sterical (entropic) stabilisation have not yet been synthesised for perfluoroalkanes. A metastable suspension could be prepared by application of ultrasonic energy. As the size of ultrasonically disrupted particle agglomerates as well as of water droplets is reduced by the energy applied to the suspension a higher resolution could probably be achieved using a very powerful ultrasound source.

Although, on the one hand, the water droplets pose a problem with respect to resolution and particle agglomeration, they offer, on the other hand, the possibility of being used as containers for transporting particles, which are not or not sufficiently charged in nonpolar oils. Furthermore, nanoparticles can be synthesised directly within the water droplets, which on their part can be stabilised at defined size by microemulsion technology [Ingelsten01]. The problem of normally inevitable oxidation of nanoparticles consisting of base metals can be circumvented thereby.

Particle attachment via electrostatic attraction presents several advantages and properties, which are of great use in potential applications. First, as it is a very general approach, the method is not restricted to any specific material combinations or chemical reactions between the species to be attached and the surfaces. Furthermore, there is no principal limitation of the process scale, i.e. the method should be expandable down to charged molecules.

The major advantage of PTFE-like materials is their inertness against almost all kinds of liquids ranging from aqueous solvents over nonpolar oils to strong

acids or bases. Furthermore, PTFE is known as an electret of very long charge retention time. The dielectric constant of the film was not measured but results obtained by other groups indicate that it is lower than that of SiO_2 suggesting applications in high-frequency microelectronics, where insulating materials of low dielectric constant are sought.

The advantage of AFM-based charge writing is that positive as well as negative charges can be written and that the process is not restricted to vacuum-compatible systems. Additionally, a large number of suitable electrets is known allowing a flexible choice with respect to the requirements of the particular system.

Even though parallel particle attachment is very fast, the disadvantage of using AFM-based charge writing still lies in the slow scanning speed. The generation of a charge pattern of the order of 1000 μm^2 takes several minutes the speed being limited rather by the usual AFM controller bandwidth than by the pulse duration of the order of μs. This difficulty could be overcome in the future by high-speed AFM systems [Schitter01] and/or by using parallel tip arrays [Vettiger00].

Due to the variability of the concept numerous extensions and applications are conceivable. Nanosized metal particles could be deposited and subsequently be molten in a sintering process to form a continuous metal line, which could by used as conductive path in microelectronics. In the case of gold an advantage is that very small particles show a lower melting temperature than the bulk matter [Buffat76].

First experiments showed that the method can also be used for localised deposition of molecules by solving them in water and using ultrasonically dispersed water droplets as carriers [NaujoksPriv]. The targeted deposition of small amounts of specific biomolecules to selected locations on a substrate is useful for the fabrication of biosensors – even if full molecular resolution is not reached. Further applications are, e.g. in cell biology, where flexible fixation methods for cells are sought. Thus, the answer to the introducing question of this thesis is: yes, it can.

Appendix A

Estimation of the effective surface charge

A point charge, q_V, is located at distance d below the surface of a dielectric of dielectric constant ϵ_m (Fig. A.1).
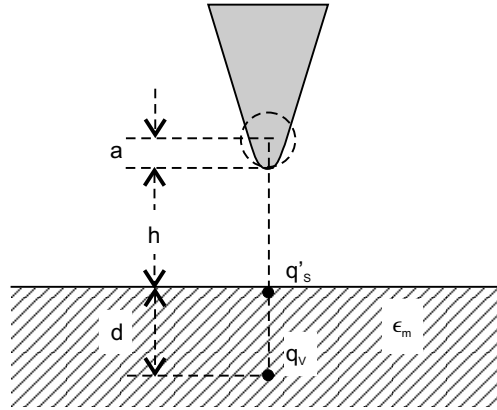
Figure A.1: **Contribution of a fixed point charge below the surface.** Effective tip radius a, tip sample distance h, penetration depth d, volume charge q_V, effective surface charge q'_S, dielectric constant of the material ϵ_m.

Using Eq. 2.17 the KFM signal of q_V becomes

$$U_{DC} = \frac{h+d}{2\pi\epsilon_0(h+d+a)^2}q'_V \tag{A.1}$$

with $q'_V = 2q_V/(1 + \epsilon_m)$ ([Jackson62], p.148) and by setting Eq. A.1 equal to Eq. 2.17 one can calculate the "effective" surface charge, q'_S, which leads to the same KFM signal as q_V, viz

$$q'_S = \frac{2(h+d)(h+a)^2}{h(h+a+d)^2(1+\epsilon_m)}q_V. \tag{A.2}$$

Fig. A.2 shows a plot of q'_S/q_V vs. d for usual lift heights. A dielectric constant
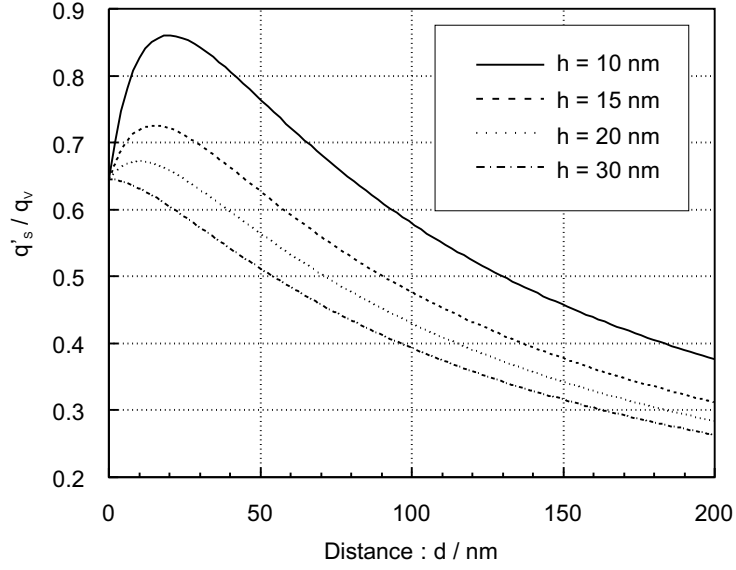
Figure A.2: **Effective surface charge.** Ratio q'_S/q_V vs. penetration depth d for different tip heights h. The maxima of the curves are at $h + d = a$.

of 2.1 and an effective tip radius of $a = 30$ nm was used here. Charge carriers which are located within the volume of the electret can be represented by surface charges of a lower magnitude depending on the distance as well as the lift height.

Appendix B

Technical details and physical data

B.1 Pulse generator

Figure B.1: **Pulse generator.** The trigger signal is fed in at A1. The delay between the falling edge of Trigger IN and the rising edge of the voltage pulse on Pulse OUT is adjusted via R1 and C1. The pulse length, t_p, is set by R2 and C2. The pulse signal passes an inverter (NOR Gate) before switching the HV FET at Pulse OUT. The dashed circuit line at the NOR Gate is not necessary for operation but the LED can be used additionally for checking the device's operation.

VS IN
0..+60V

1: Delay time between trigger and pulse output
R1 = 0..1M
C1 = 0u68
2: Pulse length t_p
R2 = 0..200k
C2 = 0u01

Trigger IN
0/+5V

74LS123

A1	V_{cc}	→ +5V
+5V → B1	R1 / C1	
+5V → Clr1	C1	
N.C. → $\overline{Q1}$	Q1	
Q2	$\overline{Q2}$	→ N.C.
C2	Clr2	→ +5V
+5V → R2 / C2	B2	→ +5V
GND	A2	

C1   R1   +5V

+5V   C2   R2

74LS123
Retriggerable Monostable
Multivibrator

74HCO2N

Y	V_{cc}	→ +5V
A	Y	→ N.C.
B	B	→ N.C.
Y	A	→ N.C.
A	Y	
B	B	
GND	A	

1   4   2   3

0k33

74HCO2N
Quadruple 2-Input Positive-
NOR Gate

1k5   1k5   1k5
1k5   1k5   1k5

1k

Pulse OUT
0/0..+60V

IRLZ14
HV FET

Pulse Generator

B.2 Electrical set-up

Equipment:			
SAM	SIGNAL ACCESS MODULE	DIGITAL INSTR.	
VS	Voltage Source	ELABO	lab source
FG	Function Generator	TABOR 8550	
PG	Pulse Generator	custom-built	(see App. B.1)
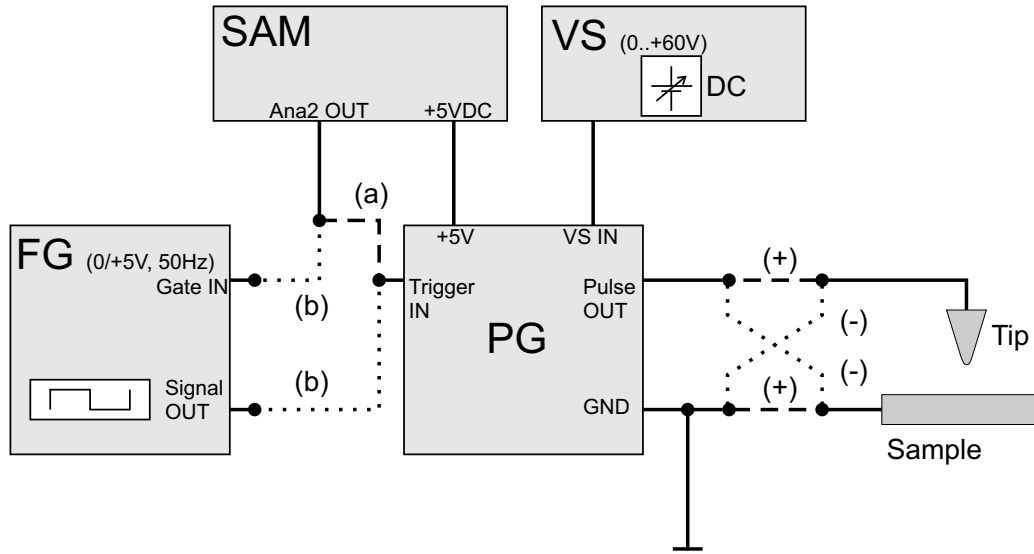
Figure B.2: **Electrical connections.** The pulse generator, PG, outputs the pulse voltage, U_p, to the conductive AFM tip. For positive charge writing (+) the tip is connected to Pulse OUT and the sample chuck is connected to GND. For negative charge writing (−), the tip is connected to GND and the sample chuck is connected to Pulse OUT. The pulse voltage is adjusted between 0 and +60V by the voltage source, VS, and the pulse length is set at PG. PG is triggered (a) directly by the signal access module, SAM, via Ana2 OUT or (b) by a continuous square signal at Signal OUT from the function generator, FG. This signal can also be gated via Ana2 OUT which is set by the LithoSetOutput-command of the AFM lithography software.

B.3   Integrator

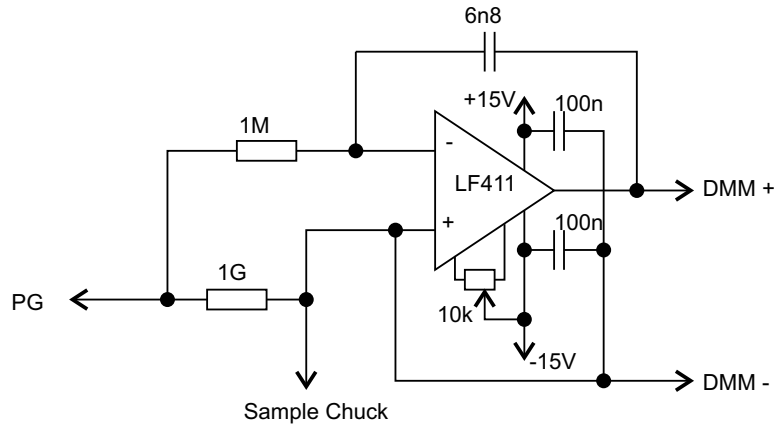Figure B.3: **Integrator.** A 1 GΩ-resistor is inserted between PG and the sample chuck. The small pulse current is measured by integrating the voltage drop at the 1 GΩ-resistor (MEGISTOR, MORGANITE INC., Dunn NC, USA) over a large number of pulses.

B.4   Source codes

The built-in lithography programming language of the NANOSCOPE III AFM was used in this work for moving the AFM tip along defined geometric paths in x-y-direction and for triggering the pulse generator. This language consists of several commands implemented by DIGITAL INSTRUMENTS in a C-library (litho.h). The program code is executed by an interpreter, which is started manually from the NANOSCOPE III software during scanning. For further details see [DI-Manual].

B.4.1   "ETH"-symbol

The program eth2.h writes the 1-μm-high and 2.5-μm-wide letters "ETH" as charge dots generated by single voltage pulses in tapping mode (see Fig. 3.5). The tip is stopped at each dot.

```
#include <litho.h>
//  writes "ETH" with letter size 1 um, recommended scan size 10 um
void main()
{
    double v,dd;
    v=10;                       //Tip velocity in um/s
    dd=0.2;                      //dot distance in um
```

```
LITHO_BEGIN
// moving tip to starting point at the lower left point of the "E"
LithoMoveZ(1,0.5);                  //moves tip 1um upwards in z-direction,
                                    //z-feedback OFF
LithoPause(10);                     //10 s pause for switching the tip from
                                    //KFM-controller to PG
LithoFeedback(TRUE);                //z-Feedback ON, tip moves to surface
LithoTranslate(-3*dd,-5*dd,v);      //to starting point

//the "E"
    LithoPulseOutput(aoAna2,5,0.001);   //triggerpulse Ana2 5V for 1 ms
    LithoPause(0.002);                  //2 ms pause so that tip doesn't move
                                        //to the next position before pulse
                                        //was applied
    LithoTranslate(-dd,0,v);            //move tip to next dot
    LithoPulseOutput(aoAna2,5,0.001);
    LithoPause(0.002);
    LithoTranslate(-dd,0,v);
    LithoPulseOutput(aoAna2,5,0.001);
    LithoPause(0.002);
    LithoTranslate(0,-dd,v);
    LithoPulseOutput(aoAna2,5,0.001);
    LithoPause(0.002);
    LithoTranslate(0,-dd,v);
    LithoPulseOutput(aoAna2,5,0.001);
    LithoPause(0.002);
    LithoTranslate(dd,0,v);
    LithoPulseOutput(aoAna2,5,0.001);
    LithoPause(0.002);
    LithoTranslate(-dd,-dd,v);
    LithoPulseOutput(aoAna2,5,0.001);
    LithoPause(0.002);
    LithoTranslate(0,-dd,v);
    LithoPulseOutput(aoAna2,5,0.001);
    LithoPause(0.002);
    LithoTranslate(dd,0,v);
    LithoPulseOutput(aoAna2,5,0.001);
    LithoPause(0.002);
    LithoTranslate(dd,0,v);
    LithoPulseOutput(aoAna2,5,0.001);
    LithoPause(0.002);
//the "T"
    LithoTranslate(3*dd,0,v);
    LithoPulseOutput(aoAna2,5,0.001);
    LithoPause(0.002);
    LithoTranslate(0,dd,v);
    LithoPulseOutput(aoAna2,5,0.001);
    LithoPause(0.002);
    LithoTranslate(0,dd,v);
    LithoPulseOutput(aoAna2,5,0.001);
    LithoPause(0.002);
    LithoTranslate(0,dd,v);
    LithoPulseOutput(aoAna2,5,0.001);
    LithoPause(0.002);
    LithoTranslate(0,dd,v);
    LithoPulseOutput(aoAna2,5,0.001);
    LithoPause(0.002);
    LithoTranslate(-dd,0,v);
    LithoPulseOutput(aoAna2,5,0.001);
    LithoPause(0.002);
    LithoTranslate(-dd,0,v);
    LithoPulseOutput(aoAna2,5,0.001);
```

```
        LithoPause(0.002);
        LithoTranslate(3*dd,0,v);
        LithoPulseOutput(aoAna2,5,0.001);
        LithoPause(0.002);
        LithoTranslate(dd,0,v);
        LithoPulseOutput(aoAna2,5,0.001);
        LithoPause(0.002);
    //the "H"
        LithoTranslate(dd,0,v);
        LithoPulseOutput(aoAna2,5,0.001);
        LithoPause(0.002);
        LithoTranslate(0,-dd,v);
        LithoPulseOutput(aoAna2,5,0.001);
        LithoPause(0.002);
        LithoTranslate(0,-dd,v);
        LithoPulseOutput(aoAna2,5,0.001);
        LithoPause(0.002);
        LithoTranslate(0,-dd,v);
        LithoPulseOutput(aoAna2,5,0.001);
        LithoPause(0.002);
        LithoTranslate(0,-dd,v);
        LithoPulseOutput(aoAna2,5,0.001);
        LithoPause(0.002);
        LithoTranslate(dd,2*dd,v);
        LithoPulseOutput(aoAna2,5,0.001);
        LithoPause(0.002);
        LithoTranslate(dd,0,v);
        LithoPulseOutput(aoAna2,5,0.001);
        LithoPause(0.002);
        LithoTranslate(0,dd,v);
        LithoPulseOutput(aoAna2,5,0.001);
        LithoPause(0.002);
        LithoTranslate(0,dd,v);
        LithoPulseOutput(aoAna2,5,0.001);
        LithoPause(0.002);
        LithoTranslate(0,-3*dd,v);
        LithoPulseOutput(aoAna2,5,0.001);
        LithoPause(0.002);
        LithoTranslate(0,-dd,v);
        LithoPulseOutput(aoAna2,5,0.001);
        LithoPause(0.002);
    LithoMoveZ(1,0.5);              //Tip 1 um upwards, z-feedback OFF
    LithoPause(10);                 //10 s pause for switching the tip from
                                    //PG to KFM-controller
    LITHO_END
}
```

B.4.2   Grid line pattern

The program `20u_1u0.h` writes twenty 20-μm-long grid lines with a pitch of ca. 1 μm. The charge dots are generated continuously during the tip travel at $v_T = 10$ μm/s and 50 Hz pulse frequency in tapping mode (see Fig. 4.8(a)).

```
#include <litho.h>
//  20 horizontal charge lines (length 20um) on 40um scansize
//  with distance 1 um
void main()
{
    int i,o;
```

73

```
    o=20;                         //number of lines

    LITHO_BEGIN
    LithoMoveZ(1,0.5);            //moves tip 1um upwards in z-direction,
                                  //z-feedback OFF
    LithoPause(10);               //10 s pause for switching the tip from
                                  //KFM-controller to PG
    LithoFeedback(TRUE);          //z-Feedback ON, tip moves down to surface
    LithoTranslate(-10,10,24);    //to starting point top left


    for (i=1;i<=o;i++)
        {
        LithoSetOutput(aoAna2,5);       //Sets SAM output Ana2 OUT to +5V
                                        //and thereby turns ON the trigger
                                        //signal from FG
        LithoTranslate(20,0,10);        //tip travels 20 um to the right
                                        //at tip velocity 10 um/s
        LithoSetOutput(aoAna2,0);       //Sets SAM output Ana2 OUT to 0V
                                        //and thereby turns OFF the trigger
                                        //signal from FG
        LithoTranslate(-20,-1,10);      //tip travels to next starting point
        }
    LithoMoveZ(1,0.5);            //Tip 1 um upwards, z-feedback OFF
    LithoPause(10);               //10 s pause for switching the tip from
                                  //PG to KFM-controller

    LITHO_END
}
```

B.4.3 25-dot-pattern

The program `5x5_puls.h` writes 25 charge dots in 5 rows at 5 dots each with spacings of about 1 μm in tapping mode. The tip is stopped at each dot (see Fig. 3.6).

```
#include <litho.h>
//  5 rows with 5 dots each row on 10 um scansize
void main()
{
    int i,j,o;
    double v;
    o=5;                          //number of rows
    v=10;                         //Tip velocity in um/s

    LITHO_BEGIN
    // moving tip to starting point
    LithoMoveZ(1,0.5);            //moves tip 1um upwards in z-direction,
                                  //z-feedback OFF
    LithoPause(10);               //10 s pause for switching the tip from
                                  //KFM-controller to PG
    LithoFeedback(TRUE);          //z-Feedback ON, tip moves down to surface
    LithoTranslate(-2,2,v);       //to starting point
    // outer for loop for rows
    for (j=1;j<=o;j++)
    {
        for (i=1;i<=o;i++)        //inner for loop for single dots
        {
            LithoPulseOutput(aoAna2,5,0.001);   //triggerpulse Ana2 5V for 1 ms
            LithoPause(0.002);                  //2 ms pause so that tip doesn't
```

```
                                          //move to the next position
                                          //before pulse was applied
          LithoTranslate(1,0,v);          //1 um to the right
      }
      LithoTranslate(-5,-1,v);   //1 um downward, 5um to the left
      LithoPause(10);            //10 sec pause for adjusting tip voltage
   }
   LithoMoveZ(1,0.5);          //Tip 1 um upwards, z-feedback OFF
   LithoPause(10);             //10 s pause for switching the tip from
                               //PG to KFM-controller
   LITHO_END
}
```

B.5   Physical data

B.5.1   Particles and suspensions

	(1)	(2)	(3)	(4)
Particle material	SiO_2	SiO_2	SiO_2	Au
Diameter	1.5 μm	290 nm	50 nm	21 nm
Standard deviation	n.s.	30 nm	10 nm	2 nm
Form	dry	aq. susp.	aq. susp.	aq. susp.
Concentration (weight-%)	100	10	5.34	n.s.
Concentration (number/ml)	-	$4.12 \cdot 10^{12}$	$4.19 \cdot 10^{14}$	$5 \cdot 10^{11}$
Art.-#	SS04N	SS02N	24040	G1652

Suppliers: (1) & (2) = BANGS LABORATORIES INC., Fishers IN, USA, (3) = POLYSCIENCES INC., Warrington PA, USA, (4) = SIGMA-ALDRICH CORP., St. Louis MO, USA.

B.5.2   Solvents

	PFD	FC-77	Water	Heptane
Chemical formula	$C_{10}F_{18}$	-	H_2O	n-C_7H_{16}
Electrical resistivity ρ/Ωcm	$1 \cdot 10^{17}$	$1.9 \cdot 10^{15}$	$18 \cdot 10^6$	$1 \cdot 10^{16}$
Relative dielectric constant ϵ_r	1.863	1.86	81	1.924
Density (water=1)	1.908	1.78	1	0.6837
Refractive index n	1.31	1.28	1.33	1.39
Surface tension $\sigma/(10^{-3}$N/m)	17.6	15	72.75	20
Boiling point $T_B/°$C	142	97	100	98.4
Dyn. viscosity $\eta/(10^{-3}$Ns/m$^2)$	5.1	1.4	1.0	4.1
Vapour pressure $p_V/$mbar	8.8	56	23.3	61

Suppliers: PFD = FLUOROCHEM LTD., Old Glossop, UK. FC-77 = INTERELEC ELECTRONICS AG, Rüschlikon, CH (Manufacturer: 3M COMPANY, St.Paul, USA). Heptane = SIGMA-ALDRICH CORP., St. Louis MO, USA, for the analytical grade, ETH Chemistry Dept. for the technical grade.

List of Figures

List of Tables

References

[Barrett91] A.C. Barrett, C.F. Quate, *Charge storage in a nitride-oxide-silicon medium by scanning capacitance microscopy,* J APPL PHYS 70 (5): 2725-2733, 1991.

[Belaidi98] S. Belaidi, F. Lebon, P. Girard, G. Leveque, S. Pagano, *Finite element simulations of the resolution in electrostatic force microscopy,* APPL PHYS A 66: S239-S243, Part 1, Suppl. S, 1998.

[Broers96] A.N. Broers, A.C.F. Hoole, J.M. Ryan, *Electron beam lithography - Resolution limits,* MICROELECTRON ENG 32 (1-4): 131-142, 1996.

[Buffat76] P. Buffat, J.P. Borel, *Size effect on the melting temperature of gold particles,* PHYS REV A 13 (6): 2287-2298, 1976.

[Castle97] G.S.P. Castle, *Contact charging between insulators,* J ELECTRO-STAT 40-1: 13-20, 1997.

[Coehn09] A. Coehn, U. Raydt, *Über die quantitative Gültigkeit des Ladungsgesetzes für Dielektrika,* ANN PHYS 4.Folge (30): 777-804, 1909.

[DI-Manual] Command Reference Manual, Version 4.10, NanoScope SPM Systems, DIGITAL INSTRUMENTS, INC., Santa Barbara CA, USA.

[Eigler90] D.M. Eigler, E.K. Schweizer, *Positioning single atoms with a scanning tunneling microscope,* NATURE 344 (6266): 524-526, 1990.

[Ertl74] G. Ertl, J. Küppers, *Low energy electrons and surface chemistry,* Verlag Chemie, Weinheim, 1974.

[Feder76] J. Feder, *Storage and examination of high-resolution charge images in Teflon foils,* J APPL PHYS 47 (5): 1741-1745, 1976.

[Feynman59] R.P. Feynman, *There's plenty of room at the bottom,* Talk given at the annual meeting of the American Physical Society, December 29, 1959 at the California Institute of Technology. Transcript available under `http://www.zyvex.com/nanotech/feynman.html` as of May 16, 2002.

[Fudouzi97] H. Fudouzi, M. Kobayashi, M. Egashira, N. Shinya, *An arrangement of micrometer-sized powder particles by electron beam drawing,* ADV POWDER TECHNOL 8 (3): 251-262, 1997.

[Fujihira99] M. Fujihira, *Kelvin probe force microscopy of molecular surfaces,* ANNU REV MATER SCI 29: 353-380, 1999.

[Hayward00] R.C. Hayward, D.A. Saville, I.A. Aksay, *Electrophoretic assembly of colloidal crystals with optically tunable micropatterns,* NATURE 404 (6773): 56-59, 2000.

[Hiemenz97] P.C. Hiemenz, R. Rajagopalan, *Principles of colloid and surface chemistry,* Dekker Inc., New York, 3rd ed. rev. and exp., 1997.

[Ingelsten01] H.H. Ingelsten, R. Bagwe, A. Palmqvist, M. Skoglundh, C. Svanberg, K. Holmberg, D.O. Shah, *Kinetics of the formation of nano-sized platinum particles in water-in-oil microemulsions,* J COLLOID INTERF SCI 241 (1): 104-111, 2001.

[Jackson62] J.D. Jackson, *Classical electrodynamics,* Wiley & sons, Inc., New York, 2nd ed., 1962.

[Jacobs97] H.O. Jacobs, H.F. Knapp, S. Müller, A. Stemmer, *Surface potential mapping: A qualitative material contrast in SPM,* ULTRAMICROSCOPY 69 (1): 39-49, 1997.

[Jacobs98] H.O. Jacobs, P. Leuchtmann, O.J. Homan, A. Stemmer, *Resolution and contrast in Kelvin probe force microscopy,* J APPL PHYS 84 (3): 1168-1173, 1998.

[Jacobs99.1] H.O. Jacobs, A. Stemmer, *Measuring and modifying the electric surface potential distribution on a nanometre scale: A powerful tool in science and technology,* SURF INTERFACE ANAL 27 (5-6): 361-367, 1999.

[Jacobs99.2] H.O. Jacobs, *Methods to measure and modify electrical properties on a nanometer scale and their applications in science and technology,* Diss. (Ph.D. thesis) Techn. Wiss. ETH Zürich, Nr. 13016, 1999.

[Jacobs99.3] H.O. Jacobs, H.F. Knapp, A. Stemmer, *Practical aspects of Kelvin probe force microscopy,* REV SCI INSTRUM 70 (3): 1756-1760, 1999.

[Jacobs01] H.O. Jacobs, G.M. Whitesides, *Submicrometer patterning of charge in thin-film electrets,* SCIENCE 291 (5509): 1763-1766, 2001.

[Jones95] T.B. Jones, *Electromechanics of particles,* Cambridge Univ. Press, New York, 1995.

[Jung95] T.A. Jung, A. Moser, H.J. Hug, D. Brodbeck, R. Hofer, H.R. Hidber, U.D. Schwarz, *The atomic force microscope used as a powerful tool for machining surfaces,* ULTRAMICROSCOPY 42: 1446-1451 Part B, 1992.

[Junno95] T. Junno, K. Deppert, L. Montelius, L. Samuelson, *Controlled manipulation of nanoparticles with an atomic force microscope,* APPL PHYS LETT 66 (26): 3627-3629, 1995.

[Keithley98] J. Yeager, M.A. Hrusch-Tupta (eds.), *Low level measurements,* KEITHLEY INSTRUMENTS, INC., Cleveland OH, USA, 5th ed., 1998.

[Kikukawa95] A. Kikukawa, S. Hosaka, R. Imura, *Silicon pn junction imaging and characterizations using sensitivity enhanced Kelvin probe force microscopy,* APPL PHYS LETT 66 (25): 3510-3512, 1995.

[KnappPriv] H.F. Knapp, private communication.

[Knapp98] H.F. Knapp, R. Guckenberger, A. Stemmer, *AFM Imaging of biological samples using hydrophobic tips,* PROBE MICROSCOPY 1: 247-257, 1998.

[Knapp99] H.F. Knapp, A. Stemmer, *Preparation, comparison and performance of hydrophobic AFM tips,* SURF INTERFACE ANAL 27 (5-6): 324-331, 1999.

[Knapp02] H.F. Knapp, P. Mesquida, A. Stemmer, *Imaging the surface potential of active purple membrane,* SURF INTERFACE ANAL 33 (2): 108-112, 2002.

[Kobayashi98] M. Kobayashi, H. Fudouzi, M. Egashira, N. Shinya, *Assemblage of particles for intelligent materials,* SMART MATER STRUCT 7 (4): 496-501, 1998.

[Kressmann96] R. Kressmann, G.M. Sessler, P. Günther, *Space-charge electrets,* IEEE T DIELECT EL IN 3 (5): 607-623, 1996.

[Krinke01] T.J. Krinke, H. Fissan, K. Deppert, M.H. Magnusson, L. Samuelson, *Positioning of nanometer-sized particles on flat surfaces by direct deposition from the gas phase,* APPL PHYS LETT 78 (23): 3708-3710, 2001.

[Mamin92] H.J. Mamin, D. Rugar, *Thermomechanical writing with an atomic force microscope tip,* APPL PHYS LETT 61 (8): 1003-1005, 1992.

[Maoz99] R. Maoz, S.R. Cohen, J. Sagiv, *Nanoelectrochemical patterning of monolayer surfaces: Toward spatially defined self-assembly of nanostructures,* ADV MATER 11 (1): 55-61, 1999.

[Maynor01] B.W. Maynor, Y. Li, J. Liu, *Au "ink" for AFM "Dip-Pen" Nanolithography,* LANGMUIR 17 (9): 2575-2578, 2001.

[Mort89] J. Mort, *The anatomy of xerography: its invention and evolution,* McFarland, London, 1989.

[Myers99] D. Myers, *Surfaces, interfaces, and colloids,* Wiley-VCH, New York, 2nd ed., 1999.

[NaujoksPriv] N. Naujoks, private communication.

[Nonnenmacher91] M. Nonnenmacher, M.P. O'Boyle, H.K. Wickramasinghe, *Kelvin probe force microscopy,* APPL PHYS LETT 58 (25): 2921-2923, 1991.

[Oyama99] Y. Oyama, Y. Majima, M. Iwamoto, *Analysis of scanning probe used for simultaneous measurement of tunneling current and surface potential,* J APPL PHYS 86 (12): 7087-7093, 1999.

[Piner99] R.D. Piner, J. Zhu, F. Xu, S.H. Hong, C.A. Mirkin, *"Dip-Pen" Nanolithography,* SCIENCE 283 (5402): 661-663, 1999.

[Sarid94] D. Sarid, *Scanning force microscopy,* Oxford Univ. Press, New York, rev. ed., 1994.

[Schitter01] G. Schitter, P. Menold, H.F. Knapp, F. Allgöwer, A. Stemmer, *High performance feedback for fast scanning atomic force microscopes,* REV SCI INSTRUM 72 (8): 3320-3327, 2001.

[Schonenberger92] C. Schönenberger, *Charge flow during metal-insulator contact,* PHYS REV B 45 (7): 3861-3864, 1992.

[Sessler87] G.M. Sessler (Ed.), *Electrets,* (Springer topics in applied physics Vol.33), Springer Verlag, Berlin, 2nd ed., 1987.

[Stern88] J.E. Stern, B.D. Terris, H.J. Mamin, D. Rugar, *Deposition and imaging of localized charge on insulator surfaces using a force microscope,* APPL PHYS LETT 53 (26): 2717-2719, 1988.

[Sugawara94] Y. Sugawara, Y. Fukano, T. Uchihashi, T. Okusako, S. Morita, Y. Yamanishi, T. Oasa, T. Okada, *Atomic-force microscopy studies of contact-electrified charges on silicon-oxide film,* J VAC SCI TECHNOL B 12 (3): 1627-1630, 1994.

[Uhlig00] M. Uhlig, A. Bertz, M. Rennau, S.E. Schulz, T. Werner, T. Gessner, *Electrical and adhesion properties of plasma-polymerised ultra-low k dielectric films with high thermal stability,* MICROELECTRON ENG 50 (1-4): 7-14, 2000.

[VanderBiest99] O.O. Van der Biest, L.J.Vandeperre, *Electrophoretic deposition of materials,* ANNU REV MATER SCI 29: 327-352, 1999.

[Vettiger00] P. Vettiger, M. Despont, U. Drechsler, U. Dürig, W. Häberle, M.I. Lutwyche, H.E. Rothuizen, R. Stutz, R. Widmer, G.K. Binnig, *The "Millipede" - More than one thousand tips for future AFM data storage,* IBM J RES DEV 44 (3): 323-340, 2000.

[Wicki01] A. Wicki, *Charakterisierung von PECVD Fluorkohlenstoffbeschichtungen,* Diplomarbeit (diploma work) Inst. f. Robotik, ETH Zürich.

[Wright98] W.M.D. Wright, D.G. Chetwynd, *Can charge writing aid nanotechnological manipulation?* NANOTECHNOLOGY 9 (2): 133-142, 1998.

Curriculum Vitae

Personal data:

Name:	Patrick Mesquida
Date of birth:	5 April 1971
Place of origin:	Wallerfangen, Germany
Nationality:	German & French

Education:

1977-1981	Grund- und Hauptschule (Primary School)
	Wallerfangen, Germany
1981-1990	Deutsch-Französisches-Gymnasium (Secondary school)
	Saarbrücken, Germany, Degree: Abitur
1990-1992	Zivildienst (Alternative military service), Saarbrücken
1992-1998	Universität des Saarlandes (Saarland University)
	Saarbrücken, Germany
	Degree: Diploma (Dipl.-Phys.) in physics
1999-2002	Nanotechnology Group
	Eidgenössische Technische Hochschule Zürich
	(Swiss Federal Institute of Technology)
	Ph.D. in the field of Nanotechnology
	Thesis advisors: Prof. Dr. A. Stemmer (ETH Zürich)
	and Prof. Dr. D. Poulikakos (ETH Zürich)